Detection of Oxyanion Adsorption at the Silica-Aqueous Interface using Total Internal Reflection (TIR)-Raman Spectroscopy

Thesis

Presented in Partial Fulfillment of the Requirements for the Degree Master of Science in the Graduate School of The Ohio State University

By

Brant M. Finzer, B.S.

Graduate Program in Chemistry

The Ohio State University

2014

Master's Examination Committee:

Prof. Dr. Heather C. Allen, Advisor

Prof. Dr. Claudia Turro

ABSTRACT

Total internal reflection (TIR)-Raman spectroscopy was used to investigate the adsorption of selenate and selenite oxyanions at the silica-aqueous interface over the pH range 5-7. If adsorption were to occur, the symmetry of the T_d selenate oxyanion would be reduced to either that of C_{3v} or C_{2v} corresponding to a monodentate or bidentate binding geometry respectively. This would cause the symmetric stretching mode in the Raman spectrum to split into two or three separate peaks respectively. It was determined that the peak corresponding to the symmetric stretching mode did not split, therefore no adsorption occurred. This provides insight to the potential mobility of selenate in the environment as adsorption to silica would greatly impact mobility through the Earth's crust.

DEDICATION

This thesis is dedicated to my parents.

ACKNOWLEDGMENTS

I would first like to thank my advisor Dr. Heather C. Allen for her guidance and support in my graduate studies. I would also like my colleagues in the Allen Lab. I would especially like to thank Dr. Dominique Verreault for the countless times I went to him for assistance with research or helping me to organize my thoughts in the writing of this thesis.

VITA

October 28th, 1989 .....Born – Dover, Ohio

2008 – 2012 .....B.S. Chemistry, Shawnee State University
Portsmouth, Ohio, USA

2012 – 2014 .....Graduate Teaching Associate/Graduate Research Associate, Department of Chemistry and Biochemistry, The Ohio State University – Columbus, Ohio, USA

FIELD OF STUDY

Major Field: Chemistry

TABLE OF CONTENTS

LIST OF FIGURES

LIST OF TABLES

LIST OF ABBREVIATIONS AND SYMBOLS

Abbreviations

ACS	American Chemical Society
ATR	Attenuated Total Reflection
BD	Beam Dump
CCD	Charge Coupling Device
DFTMD	Density Functional Theory Molecular Dynamics
EXAFS	Extended X-ray Adsorption Fine Structure
FL	Focusing Lens
FWHM	Full Width at Half Maximum
HAO	Hydrated Aluminum Oxide
HFO	Hydrated ferric Oxide
I	Iris
IR	Infrared
IS	Inner-Sphere
LPF	Long-Pass Filter
M	Mirror
NDF	Neutral Density Filter
NMR	Nuclear Magnetic Resonance

OBJ	Objective
OS	Outer-Sphere
PZC	Point of Zero Charge
TIR	Total Internal Reflection
XSW	X-ray Standing Wave

Symbols

α	Polarizability
α_0	Equilibrium Polarizability
β	Decay Factor
ε_0	Permittivity of Free Space
λ_0	Excitation Wavelength
μ_{in}	Induced Dipole Moment
ν_x	Frequency of "*x*"
ν_n	Raman active mode "*n*" (*n* is an integer)
ν_x	Vibrational energy level "*x*"
ψ	Wavefunction
θ_t	Transmission Angle
θ_i	Incident Angle
θ_c	Critical Angle
σ_d	Symmetry Operation: Dihedral Reflection Plane
σ_v	Symmetry Operation: Vertical Reflection Plane
τ	All space
ω_{rn}	Frequency of the Transition Between *r* and *n*
A_1	Symmetry Species
A_2	Symmetry Species

B_1	Symmetry Species
B_2	Symmetry Species
C	Concentration
C_2	Symmetry Operation: Two-fold Rotation
C_3	Symmetry Operation: Three-fold Rotation
C_{2v}	Two-fold Rotation Cyclic Point Group Label
C_{3v}	Three-fold Rotation Cyclic Point Group Label
D_p	Probing Depth
E	Symmetry Species, Symmetry Operation: Identity
E	Electric field
E_0	Electric Field at Time Zero
E_m	Amplitude of the electromagnetic wave
$E_t(z)$	Transmitted Electric Field as a Function of Distance
h	Planck's constant, Order of the Point Group
$\hbar$	Reduced Plank's Constant
$\widehat{H'}$	1st Order Correction to the Hamiltonian
I_{as}	Intensity of Anti-Stokes transition
I_s	Intensity of Stokes transition
k_b	Boltzmann Constant
k_t	Wave Vector of the Transmitted Wave
L_d	Decay Length
$M_{10}(t)$	1st Order Correction to the Transition Dipole Moment

n_t	Index of Refraction of the Transmission Medium
n_i	Index of Refraction of the Incident Medium
r	Internuclear Distance
R	Raman Transition Moment
R^2	Goodness of Fit
r_e	Equilibrium Internuclear Distance
r_m	Maximum Internuclear Distance
r_p	Fresnel Coefficient: Reflectance *p*-Polarized
r_s	Fresnel Coefficient: Reflectance *s*-Polarized
S_4	Symmetry Operation: Four-fold Rotation followed by Reflection in a Plane Normal to the Rotation Axis
t	Time
T	Temperature
T_1	Symmetry Species
T_2	Symmetry Species
T_d	Tetrahedral Point Group Label
t_p	Fresnel Coefficient: Transmission *p*-Polarized
t_{px}	Total Internal Reflection Complex Transmission Coefficient
t_{sy}	Total Internal Reflection Complex Transmission Coefficient
t_{pz}	Total Internal Reflection Complex Transmission Coefficient
t_s	Fresnel Coefficient: Transmission *p*-Polarized
W_g	Gaussian Width

W_l	Lorentzian Width
$\mathbf{X}$	Orthogonal Transform Matrix
y_0	*Y*-intercept
z	Distance

CHAPTER 1: INTRODUCTION

1.1 Environmental Contamination

Water in an area of land takes on some characteristics of the local environment as it absorbs through the soil and reacts with minerals, gases, and organics present. This process continues as the water seeps into the water table and flows into the aquifer. Groundwater evolves depending on the types of reactions that have occurred between the different solid and gaseous phases it has encountered; and in the United States is a huge source of drinking water, water for irrigation, and used for industry. Today, geochemistry plays an important role understanding migration of contaminants, characterizing natural systems, and designing programs to remediate existing concerns. If one were to neglect the geochemical importance of contaminants in environmental waters, it could oversimplify the situation and cause serious errors in conclusions made about the impact of contamination on the environment.[1] This problem becomes evident as the water getting into the environment carries with it dangerous contaminants from any of a number of anthropogenic sources. This water will eventually find its way to aquifers that supply water sources for human activity, and it will bring with it any soluble pollutant it has encountered that has not been adsorbed by various components of Earth's crust. Aquifers are present in all types of rock, whether flowing between granules of sedimentary rocks, or in fractures

through igneous and metamorphic rock, and minerals as crystalline solids and amorphous solids are the components of these rocks, which make up the Earth's crust.

1.2 Importance of Oxyanion Adsorption to Mineral Oxides

The major source of dissolved species in groundwater is solid material the water has been in contact with. Solids may also adsorb materials from groundwater acting as a sink for contaminants, providing a mechanism that controls the movement of contaminants dissolved in the water; thereby limiting the amount in solution. Although, almost every element on the periodic table is found in some solids in the crust, the major constituents are limited to very few; silicon, aluminum, and iron.[1] While there are other elements that make up a large portion of the crust, they are also commonly found in groundwater. The three listed above are not typically found in groundwater as the minerals they form have low solubility in aqueous environments.[1] Mineral oxides are of particular importance as they not only are in equilibrium with an aquifer environment, but as they also form very reactive surfaces on which aqueous species may adsorb. Silica, aluminum, and iron oxides being the primary mineral oxides found in the crust are of obvious importance as they make up a majority of the reactive surfaces present in the environment to control mobility of dissolved species.

It is the mobility of contaminants that is of particular interest; how far will a pollutant travel? Will it make it into rivers and lakes, what about drinking water? If some contaminant is not adsorbed by minerals in the ground, it will travel as far as the water carrying it will take it. It is entirely possible for contaminants to build to dangerous levels

in not only groundwater, but even in rivers and lakes. Some contaminants may be fairly benign, however, the problem lies in whether some pollutant is toxic. If so, then the issue becomes determining the source of the toxic pollutant, figuring out how mobile it is, and how to remove the pollutant. Sources for toxic pollutants include agriculture, coal operations, mining operations, fracking, oil drilling, etc… These toxic pollutants include arsenic, chromium, and selenium; existing in an oxidized state (AsO_4^{3-}, CrO_4^{2-}, and SeO_3^{2-}/SeO_4^{2-}).

1.3 Previous Studies on the Sorption of Oxyanions to Minerals/Metal Oxides

The study of adsorption to various mineral and metal oxides covers a broad range of research. While many interesting topics have been inspected, many are beyond the scope of this work. Herein, the discussion will focus on the study of the sorption of anionic species to mineral surfaces. There are many more studies covering oxyanion sorption to various metal oxides/minerals; it is not possible to reference them all here, however, the following is a brief overview of some of these studies.

Recent works such as the work of Perez et al. modelling the sorption of oxyanions on ferralic soils are more along the lines of the present study.[2-3] They worked on improving current surface complexation models, validating improvements with phosphate (PO_4^{3-}) studies, and extending the technique to study chromate (CrO_4^{2-}), selenate (SeO_4^{3-}), molybdate (MoO_4^{2-}), and arsenate (AsO_4^{3-}).[2-3] They worked to model the effects of pH, ionic strength, etc. on the mobility of these ions in soils with a high iron content. They also determined the order of anion affinity to be $PO_4^{3-} \approx AsO_4^{3-} > CrO_4^{2-} > MoO_4^{2-} > SeO_4^{2-}$.[3]

Neupane et al. recently studied the individual and competitive kinetics of the sorption of arsenate and phosphate on ferrihydrite.[4] It was determined that each ion initially adsorbed rapidly, then sorption slowed down. Both anions showed some limited ability to remove the other after the system was allowed to equilibrate, and during competitive experiments, arsenate was the preferred species.[4] Vasileva et al. studied the adsorption of Cr^{6+} oxyanions onto pure anatase (TiO_2) and an anatase sample that was treated with H_2O_2.[5] They studied the adsorption as a function of pH and determined that adsorption increased with decreasing pH.[5] It was also determined that pretreatment with H_2O_2 increased the sorption of the oxyanions.[5] A study by Stachowicz modeled the competitive interactions of arsenite (AsO_2^-) and arsenate, As (III) and As (V) respectively, with Ca^{2+}, Mg^{2+}, PO_4^{3-}, and CO_3^{2-} onto goethite.[6] It was determined that the two cations have no effect for arsenite, and expect a promoting effect for sorption of arsenate.[6] It was also determined that adsorbed phosphate ions strongly interact with both arsenic oxyanions.[6] Upon investigating multi-component systems, it was again determined that phosphate played the major role in regulating arsenite and arsenate.[6]

In 2004, Lefèvre published a review of the use of attenuated total reflection–infrared (ATR-IR) spectroscopy for the study of inorganic ion adsorption to mineral oxides and hydroxides. For sulfate adsorption, it was determined that sorption to goethite occurs via inner-sphere (IS) and outer-sphere (OS) adsorption; OS dominates for sorption to Cr(III) oxy-hydroxide; hematite sorption also occurs via a mixture of IS and OS adsorption, with IS playing a bigger role; and for anatase, the adsorption signal is attributed to IS complexation. For carbonate adsorption, the studies pointed to monodentate complexation

for all substrates considered: hydrous aluminum oxide (HAO), hydrous ferric oxide (HFO), goethite, hematite, and aged γ-alumina. Arsenate sorption on amorphous ferric oxide was also studied; the data suggested a bidentate sorption structure.[7]

1.4 Silica and Selenium

1.4.1 The Silica Surface

Among other various mineral and metal oxides, silica plays an important part as it is the most abundant mineral in the Earth's crust. As such, silica is the mineral which comes in contact with water the most in the Earth's crust. Studying the interfacial interactions of silica with aqueous solutions may then provide a wealth of information for the fate of dissolved species. It is also important to understand the type of surface sites available on any given metal oxide, as they will determine the type of bonding that may occur. There are a number of various surface sites exhibited on silica, the most prevalent being silanol (Si-OH). Other sites include the siloxy anion ($Si\text{-}O^-$), siloxane (Si-O-Si), and a protonated silanol ($SiOH_2^+$).[8] There are also various types of silanol groups; they may be isolated, vicinal, and geminal.[8] A diagram of these various surface sites is given in Figure 1.1.

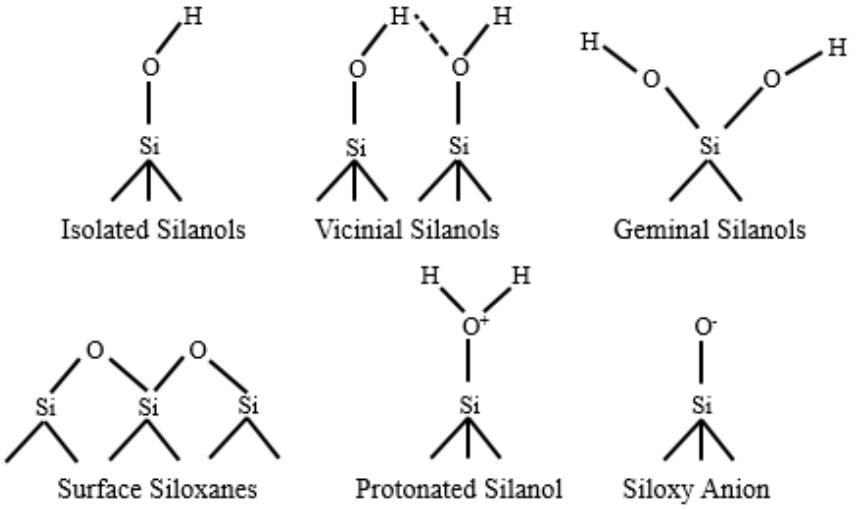

Figure 1.1: Diagram of the various surface sites possible at the silica-aqueous interface.

For the current study, only three types of surface sites were considered; protonated silanol, silanol, and the siloxy anion, no distinctions between the types of silanol were made. Utilizing pKa values from the recent work of Sulpizi et al., a speciation curve was made for the silica surface. The speciation curve is shown below in Figure 1.2. The values used for the pKa are -5 for the protonated silanol, and 8.5 for silanol.[9] The pKa values were determined by Sulpizi utilizing density functional theory molecular dynamics (DFTMD) calculations. In actuality they determined that there are two types of silanol present, so-called "out-of-plane" silanols with a pKa of 5.6, and "in-plane" silanols whose pKa is 8.5. The pKa for in-plane silanols was the value chosen as it was shown by Ong et al. that there is an approximately 1:4 ratio of out-of-plane to in-plane silanol groups.[10] Leung et al. also determined pKa values for these silanol groups and they are in agreement with previous reports.[11]

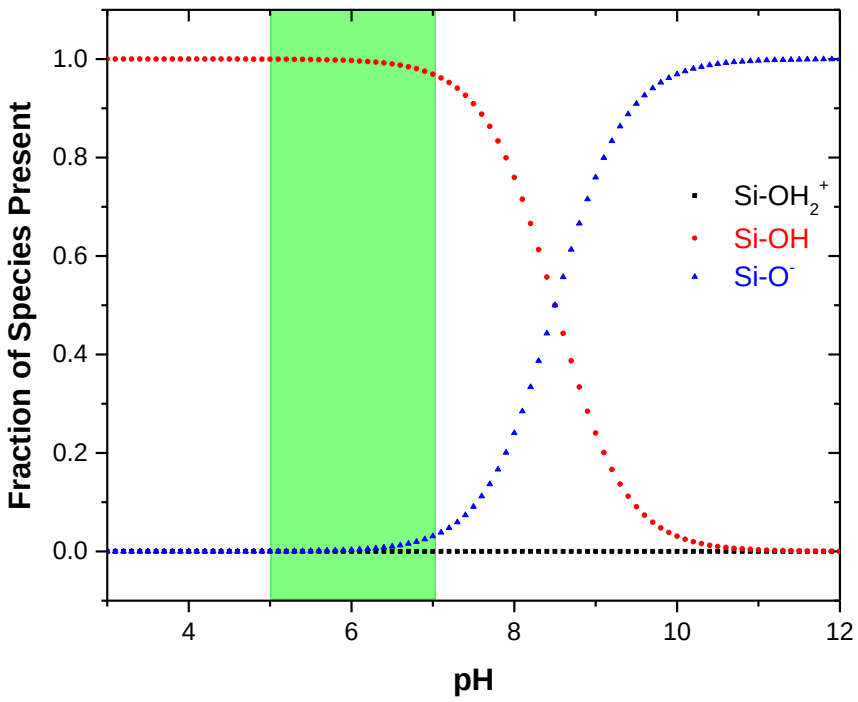

Figure 1.2: Speciation curve for silica surface sites vs pH. Note that at pH<7, >95% of surface sites exist as Si-OH.

1.4.2 Previous Studies of Adsorption on Silica

Due to its ubiquitous nature, the silica surface is one that has been extensively studied. A plethora of literature exists for the study of biologically-relevant molecules adsorbing or otherwise interacting with a silica surface. The techniques range from bulk experiments, to vibrational techniques, to nuclear magnetic resonance (NMR) spectroscopy, and even X-ray diffraction (XRD).[12] The study of these biomolecules is beyond the scope of the current study, however a recent review by Rimola et al. provides a decent place to start if one is interested in such studies.[12] A quick summary of the solution adsorption experiments covered shows that the significant research is that of adsorption of

various amino acids to the silica surface.[12] The techniques used included IR spectroscopy and NMR, and Many studies were performed via construction of adsorption isotherms.[12]

Regarding adsorption of various small inorganics, a relatively small amount of literature exists compared to the above. Of this, a fair amount of work has been dedicated to studying the interactions of water itself with the surface or its competition with various molecules/ions. Wang and co-workers demonstrated the adsorption of water from the vapor phase to be dependent on ambient conditions utilizing an interferometric optical balance.[13] It was demonstrated that adsorption of water to form a layer on the order of nanometers occurred even on a hydrophobic silica surface. Gouveia et al. demonstrated the adsorption of water by observing reproducible electric potential patterns on silica surfaces.[14] This was performed by integrating a gold electrode to the silica surface, and utilizing an atomic force microscope equipped with a Kelvin force attachment. They noted that the build-up of charge, and formation of a pattern occur much faster under relatively high humidity.[14] It was also noted that the charged and discharged states are more stable under low relative humidity.[14] Mahadevan and Garofalini showed dissociative chemisorption of water in the vapor phase to the silica surface to form silanol groups by performing molecular dynamics simulations.[15] It was also noted that water penetration and silanol production occurs approximately 8 Å below the outermost oxygen.[15]

There also exist many studies on the adsorption of various metal cations to the silica surface. Mazurenka et al. used evanescent wave cavity ring-down spectroscopy to study the sorption of colloidal gold of different particle sizes onto functionalized silica surfaces.[16] Gomoyunova et al. studied the processes of iron sorption to the oxidized silicon surface

using core-level photoelectron spectroscopy.[17] They noted that the iron penetrated below the silicon oxide layer at surface coverages below 4 monolayers, and above that, sorption occurs.[17] In their 2005 paper, Donose et al. utilized lateral force microscopy to investigate the effects of adsorption of cations on the frictional force between two silica surfaces.[18] They found that solutions of high concentration provided significant lubrication, and that smaller cations, and those with more hydration provided higher lubrication compared to larger and less hydrated ions.[18] Wang et al. studied the sorption of 36 elements to silica in relation to pH and fulvic acid concentration.[19] There is a great deal of literature on the sorption of various metals and cationic species to unmodified silica, however there is a lack of literature sorption of anionic species to silica. [20]

1.4.3 Selenium in the Environment

Environmental selenium has received much attention since the initial discovery of contaminated waters in the San Joaquin Valley of California in 1982 which resulted in the Department of the Interior initiating investigations to locate other areas plagued with water contamination problems.[21] The following is a quick summary of some of the many studies of selenium presence in the environment demonstrating the importance of studying selenium species as a whole.

In 1995, Hamilton published a study assessing the hazards that various inorganics pose to three endangered species of fish in the Green River of Utah. [22] The study was conducted on three different life stages of bonytail, razorback sucker, and the Colorado squawfish. The order of toxicity for all three life-stages and species was determined to be:

vanadium = zinc > selenite > lithium = uranium > selenate > boron.[22] It was also determined that the Colorado squawfish was 2-5 times more sensitive to selenate and selenite at the youngest life-stage studied compared to the older life-stages; the bonytail were also five times more sensitive to selenate during the earliest life-stage.[22] Studies of Ashley Creek, Utah revealed moderate hazards to wildlife for boron, selenate, selenite, and zinc.[22] In 1997, Hamilton reported a similar study for the flannelmouth sucker; the toxicity ordering is as follows: Cu > Zn > V > Se(IV) > Se(VI) > As(V) > U > B > Mo.[23] Comparison to reported concentrations for the San Juan River revealed a relatively low hazard from either oxidation state of Se.[23] In 2000, Hamilton published another report studying the razorback sucker and the bonytail, this time with a mixture of inorganics attempting to replicate irrigation run-off. It was noted that adverse effects were seen for fish with residues of copper, selenium, and zinc in their bodies; and comparison to environmental concentrations reveal a high hazard to the fish.[23] Thus, again, linking irrigation activities to the decline of these endangered species in the Green River.[23]

Geoffroy et al. published a study of the effects of selenate on the growth and photosynthesis of a species of green algae. Inhibition was observed at approximately 4.5 μM selenate, a low concentration compared to environmental levels.[24] It was also determined that selenate targets the chloroplasts affecting the electron chain of photosynthesis.[24] Duan et al. studied the distribution of selenium in the Bohai Bay, they observed average concentrations of selenite and selenate to be 0.72 and 0.36 nM, respectively.[25] They also noted that variations in the selenium concentration correlated with phytoplankton blooms, implying that selenium is important for regulating

phytoplankton production.[25] Although these concentrations were particularly low, it is noted that due to bioaccumulation, it may pose a threat to higher levels of the food chain.[25] Torres et al., in 2011, studied speciation of selenium anions under various conditions. [26] It was determined for selenate that it exists predominantly in its non-protonated form in natural waters, and selenite primarily exists as biselenite ($HSeO_3^-$). In 2011, Floor et al. studied selenium mobility and speciation in volcanic soils utilizing samples from the Mount Etna volcano. They found that not only must one consider iron oxides in attempting to determine mobility, but aluminum oxides and even some organic matter play a major role in controlling the mobilization of selenium oxyanions in these soils.[27] It was also determined that selenate dominates the speciation of selenium found in volcanic soil samples collected around the crater.[28]

1.4.4 Previous Selenium Oxyanion Sorption Studies on Mineral/Metal Oxides

The following passage is a small sample of the work that has been completed studying the sorption of selenium oxyanions to various mineral/metal oxides. For example, in 2002 Peak and Sparks investigated the binding mechanism of selenate adsorption to iron oxides and hydroxide. They made use of extended X-ray absorption fine structure (EXAFS) and ATR-IR to determine if the sorption occurred via IS or OS geometry. It was determined hematite that sorption occurred only via IS coordination, whereas for goethite and HFO, sorption was a mixture of IS and OS.[29] Yamani et al. studied the sorption of selenite and selenate on TiO_2 and nanocrystalline aluminum oxide (n-Al_2O_3), they also investigated chitosan beads impregnated with each oxide. They observed n-Al_2O_3 to have

the greatest removal of selenite and selenate, followed by the Al beads.[30] TiO_2 adsorbed approximately double the amount of selenite compared to selenate, and was less than n-Al_2O_3 for both.[30] Duc et al. investigated the sorption of selenite and selenate on apatites and iron oxides. It was found that selenate ion adsorption is much weaker than that of selenite sorption, and that the two apatites studied (hydroxyapatite and fluorapatite) have greater retention for both ions.[31] Catalano et al. made use of X-ray standing wave (XSW) measurements to observe the sorption of selenite to the hematite (100) surface. Selenite was found to adsorb primarily via bidentate bridging coordination.[32] Rovira et al. utilized batch adsorption experiments and modelling to investigate the sorption of selenite and selenate to goethite and hematite. They determined that selenite sorption onto hematite occurred via a monodentate IS complex and a mixture of a deprotonated and protonated monodentate IS complex for sorption to goethite.[33] Selenate adsorbed to hematite via a mixture of OS complexation and a monodentate IS geometry; adsorption to goethite was described with an OS geometry.[33] Recently, Goldberg investigated the sorption of selenite and selenate onto gibbsite as a function of solution ionic strength pH. [34] It was found that with increasing ionic strength, adsorption decreased for both anions with selenate having a more drastic response; this dependence suggests that each anion has some OS adsorption occurring, with selenate having a greater proportion of OS binding. It was also determined that increasing solution pH decreased anion adsorption.[34] The point of zero charge (PZC) was also determined after adsorption for each anion; these measurements showed a change in PZC suggesting an IS geometry.[34] Thus, it was concluded that a mixture of IS and OS geometries must be used to described the sorption of either anion to the gibbsite surface

from an aqueous solution.[34] Figure 1.3 depicts the monodentate and bidentate binding geometries.

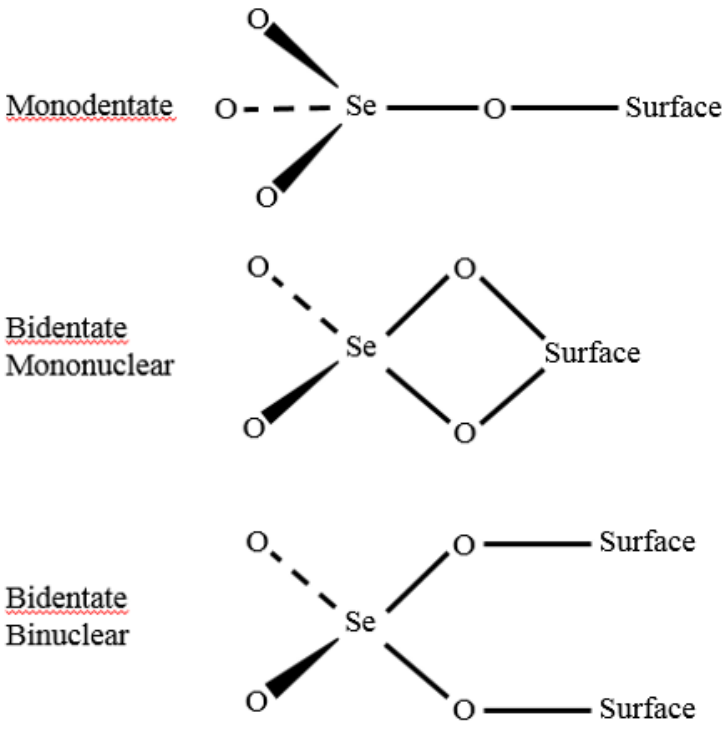

Figure 1.3: Diagram representing the geometries of monodentate and two different bidentate adsorption species.

1.5 Objectives of the Current Study

It is the objective of the current study to investigate to adsorption of selenate and selenite at the silica-aqueous interface as a function of solution pH and concentration utilizing total internal reflection (TIR-) Raman spectroscopy. It is also a goal of this study to determine the geometry through which the adsorption occurs. This study will help to elucidate the sorption capability of soils of high silica content, and may be utilized by those

wishing to construct larger mobility models to predict the mobility of selenate in such soils. This work will also form a baseline for comparison with future studies of sorption to other mineral oxides such as hematite, goethite, gibbsite, etc. To the author's knowledge this is the first attempt at spectroscopically determining the binding geometry of selenate to the silica surface.

CHAPTER 2: THEORETICAL BACKGROUND

2.1 Total Internal Reflection (TIR-) Raman Sectroscopy

2.1.1 Classical Theory of Raman Scattering

Before one can discuss TIR-Raman spectroscopy, one must first have an understanding of Raman scattering. Raman scattering may arise from the rotational and vibrational modes of a given molecule. Specifically, those modes which cause a change in the polarizability of said molecule. The polarizability of a molecule is a measure of how efficiently a given incident frequency induces a dipole in the molecule.[35] Modes which cause a change in the molecular polarizability are said to be Raman-active modes. With Brillouin scattering, Raman scattering is one type of inelastic scattering. Inelastic scattering is that during which an incident photon is absorbed promoting a molecule from the ground or first excited vibrational state to a virtual state with relaxation to either a higher or lower state than the initial. This relaxation emits a photon of either lower or higher frequency than that of the excitation photon. Thus, there are two types of Raman scattering that may occur, scattering that corresponds to a lower frequency emitted photon, called Stokes; and scattering corresponding to a higher frequency emitted photon, known as anti-Stokes. Figure 2.1 gives a simplified energy diagram depicting the two forms of Raman scattering along with elastic Rayleigh scattering.

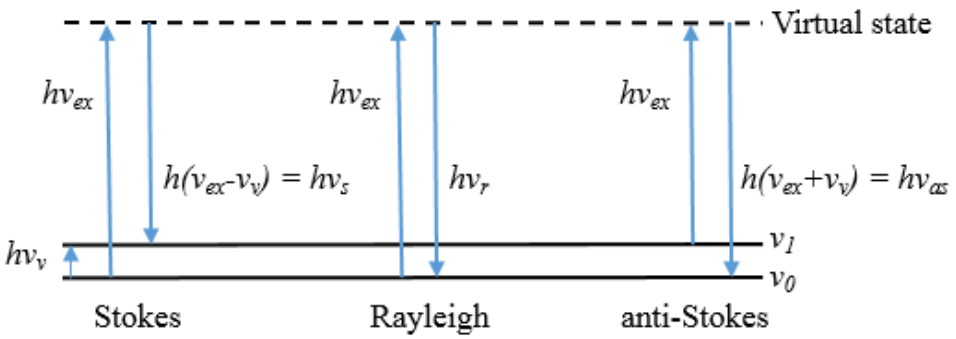

Figure 2.1: Energy level diagram depicting Stokes, Rayleigh, and anti-Stokes scatterings. In Stokes scattering, molecules absorb a photon of energy $h\nu_{ex}$ and emit a photon of energy $h(\nu_{ex}-\nu_v) = h\nu_s$. in contrast, anti-Stokes scattering emits a photon of energy $h(\nu_{ex}+\nu_v) = h\nu_{as}$.

The following is a brief classical derivation of the Raman effect.[35] Consider a laser of frequency ν_{ex} incident upon the sample, its electric field can be written as:

$$E = E_m \cos(2\pi\nu_{ex}t) \tag{2.1}$$

where E_m is the amplitude of the wave. When this wave interacts with a polarizable electron cloud it induces a dipole moment, μ_{in}:

$$\mu_{in} = \alpha E = \alpha E_m \cos(2\pi\nu_{ex}t) \tag{2.2}$$

In Eqn. 2.2, μ_{in} has units of C m, and α is the polarizability of the molecule with units of J^{-1} C^2 m^2. If one desires α to have units in m^3, simply divide by $4\pi\varepsilon_0$.

The Raman effect arises from the interaction of the normal vibrational modes with the polarizability. Polarizability varies with the internuclear distance around its equilibrium value α_0. This variation occurs according to:

$$\alpha = \alpha_0 + (r - r_e)\left(\frac{\delta\alpha}{\delta r}\right)_e + \cdots \tag{2.3}$$

where, α_0 is the polarizability at equilibrium bond distance r_e, and r is the internuclear distance. The subscript "e" on the partial derivative represents evaluation at equilibrium

bond length. The change in the bond distance varies with the frequency of a vibration ν_v according to:

$$r - r_e = r_m \cos(2\pi\nu_v t) \tag{2.4}$$

where r_m represents the maximum nuclear separation relative to equilibrium. Substituting Eqn. (2.4) into Eqn. (2.3), we obtain:

$$\alpha = \alpha_0 + r_m \cos(2\pi\nu_v t)\left(\frac{\delta\alpha}{\delta r}\right)_e \tag{2.5}$$

Substituting Eqn. (2.5) into Eqn. (2.2), we obtain an expression for the induced dipole:

$$\mu_{in} = \alpha_0 E_m \cos(2\pi\nu_{ex} t) + E_m r_m \left(\frac{\delta\alpha}{\delta r}\right)_e \cos(2\pi\nu_v t)\cos(2\pi\nu_{ex} t) \tag{2.6}$$

Using the identity for the product of two cosines:

$$\cos x \cos y = \frac{1}{2}[\cos(x+y) + \cos(x-y)] \tag{2.7}$$

leads us to construct:

$$\mu_{in} = \alpha_0 E_m \cos(2\pi\nu_{ex} t) + \frac{E_m}{2} r_m \left(\frac{\delta\alpha}{\delta r}\right)_e \cos 2\pi(\nu_{ex} + \nu_v)t$$

$$+ \frac{E_m}{2} r_m \left(\frac{\delta\alpha}{\delta r}\right)_e \cos 2\pi(\nu_{ex} - \nu_v)t \tag{2.8}$$

The first term, second, and third terms correspond to Rayleigh, anti-Stokes, Stokes scatterings respectively. While the classical derivation does predict that Raman scattering will occur, it does not account for the relative intensities between Stokes and anti-Stokes scattering. To predict this, it would be necessary to account for the relative populations of the energy levels. A quantum mechanical approach taking populations into account can accurately predict the relative intensities.

To determine the selection rules for Raman scattering, one must evaluate the transition moment:[35]

$$R = \int \psi_i^* \left[\alpha_0 + (r - r_e)\left(\frac{\delta\alpha}{\delta r}\right)_e\right]\psi_j d\tau \tag{2.9}$$

This simplifies to:

$$R = \int \psi_i^* \left[(r - r_e)\left(\frac{\delta\alpha}{\delta r}\right)_e\right]\psi_j d\tau \tag{2.10}$$

From Eqn. (2.10) it can be seen that a change in the polarizability must occur during vibration. The selection rules also predict that fundamental Raman lines occur with $\Delta v = \pm 1$, with overtones at $\Delta v = \pm 2$ being much weaker. As will be discussed later, group theory provides an easy way to determine if a vibration mode will be Raman active.

2.1.2 Corrections to Classical Theory and a Quantum Approach

As aforesaid, the classical approach does not account for the relative intensities of Stokes and anti-Stokes scattering. The problem here is that the induced dipole and the applied electric field need not be oriented in the same direction. The first problem can be accounted for with the application of Boltzmann statistics, and assuming a classical oscillator, the ratio of intensities of anti-Stokes to Stokes is given by:[36]

$$\frac{I_{as}}{I_s} = \frac{(\nu_{ex}+\nu_v)^4 e^{-h\nu_v/k_bT}}{(\nu_{ex}-\nu_v)^4} \tag{2.11}$$

The use of a classical oscillator gives a dependence on the frequency of the scattered light to the fourth power.

A classical approach also fails to account for the orientation of a molecule relative to the laboratory coordinate system. For example; consider a highly symmetric molecule such as methane, the induced dipole and the applied electric field point in the same direction. However, for less symmetric molecules this need not be the case, i.e. $\vec{\boldsymbol{E}}$ and $\vec{\boldsymbol{\mu}}_{\boldsymbol{in}}$ can point in different directions.[36] This is because the molecular response to the applied field can be different along the *X*, *Y*, and *Z*-axes of the laboratory frame. Writing the first part of Eqn. (2.2) in matrix form gives:[36]

$$\vec{\boldsymbol{\mu}}_{\boldsymbol{in}} = \boldsymbol{\alpha}\vec{\boldsymbol{E}} \tag{2.12}$$

$$\begin{pmatrix} \mu_x \\ \mu_y \\ \mu_z \end{pmatrix} = \begin{pmatrix} \alpha_{xx} & \alpha_{xy} & \alpha_{xz} \\ \alpha_{xy} & \alpha_{yy} & \alpha_{yz} \\ \alpha_{xz} & \alpha_{yz} & \alpha_{zz} \end{pmatrix} \begin{pmatrix} E_x \\ E_y \\ E_z \end{pmatrix} \tag{2.13}$$

In this notation, the polarizability becomes a 3×3 symmetric matrix called the polarizability tensor. This tensor can be simplified by working in the principle axis system of the molecule. Since the polarizability tensor is a real symmetric matrix, it is possible to construct an orthogonal transformation matrix **X** from the normalized eigenvectors of $\boldsymbol{\alpha}$.[36] The matrix **X** represents a rotation of the coordinate system into the principle axis i.e. $\boldsymbol{r'} = \boldsymbol{X^{-1}r}$. Using the similarity transform allows one to relate the diagonalized matrix and the polarizability tensor:

$$\boldsymbol{\alpha'} = \boldsymbol{X^{-1}\alpha X} \tag{2.14}$$

This new matrix contains the eigenvalues of the polarizability tensor and has the form:

$$\boldsymbol{\alpha'} = \begin{pmatrix} \alpha_{x'x'} & 0 & 0 \\ 0 & \alpha_{y'y'} & 0 \\ 0 & 0 & \alpha_{z'z'} \end{pmatrix} \tag{2.15}$$

Using a quantum mechanical approach to derive Raman theory, one uses first-order perturbation theory to find the correction to the transition dipole moment:[36]

$$\boldsymbol{M}_{10}(t) = \langle \psi_1 | \vec{\boldsymbol{\mu}} | \psi_0 \rangle \tag{2.16}$$

The first-order correction to the Hamiltonian is given as:[36]

$$\widehat{\boldsymbol{H}}' = -\vec{\boldsymbol{\mu}} \cdot \vec{\boldsymbol{E}}_0 \cos(\omega t) \tag{2.17}$$

Using time-dependent perturbation theory leads to the time-dependent first-order correction to the wavefunction as:[36]

$$\Psi_n^{(1)} = \frac{1}{2\hbar} \sum_r \psi_r^{(0)} \left(\frac{\vec{\boldsymbol{\mu}}_{rn} \cdot \vec{\boldsymbol{E}}_0}{\omega_{rn} - \omega} e^{-i(\omega_n + \omega)t} + \frac{\vec{\boldsymbol{\mu}}_{rn} \cdot \vec{\boldsymbol{E}}_0}{\omega_{rn} - \omega} e^{-i(\omega_n - \omega)t} \right) \tag{2.18}$$

with

$$\omega_{rn} \equiv {(E_r - E_n)}/{\hbar} \tag{2.19}$$

Thus, it can be shown that the expression for the oscillating transition dipole moment for a Raman transition from state *n* to *k* is given via first-order perturbation theory as:[36]

$$\boldsymbol{M}_{kn}^{(1)}(t) = \frac{e^{i(\omega_{kn} - \omega)}}{2\hbar} \sum_r \left(\frac{\vec{\boldsymbol{\mu}}_{kr} (\vec{\boldsymbol{\mu}}_{rn} \cdot \vec{\boldsymbol{E}}_0)}{\omega_{rn} - \omega} + \frac{\vec{\boldsymbol{\mu}}_{rn} (\vec{\boldsymbol{\mu}}_{kr} \cdot \vec{\boldsymbol{E}}_0)}{\omega_{rk} + \omega} \right) \tag{2.20}$$

2.1.3 Total Internal Reflection and the Critical Angle

Having established an understanding of Raman scattering, one can begin to understand TIR-Raman Spectroscopy. TIR-Raman is a variant of Raman spectroscopy in which the electric field of an evanescent wave generated at an interface is used as the excitation source. Upon striking an interface, a beam of light is split into a reflected and a transmitted beam. At the interface, the components of the electric and magnetic fields that are tangential to the surface must be continuous.[37] This allows the calculation of reflection

and transmission coefficients, *r* and *t*, for parallel and perpendicularly polarized light (termed *p* and *s*, respectively). These terms are as follows:[37]

$$r_p = \frac{\tan(\theta_i - \theta_t)}{\tan(\theta_i + \theta_t)} \tag{2.21}$$

$$t_p = \frac{2 \sin\theta_t \cos\theta_i}{\sin(\theta_i + \theta_t)\cos(\theta_i - \theta_t)} \tag{2.22}$$

$$r_s = -\frac{\sin(\theta_i - \theta_t)}{\sin(\theta_i + \theta_t)} \tag{2.23}$$

$$t_s = \frac{2 \sin\theta_t \cos\theta_i}{\sin(\theta_i + \theta_t)} \tag{2.24}$$

where θ_i and θ_t are the incident and the transmittance angles, respectively. θ_t may be calculated using Snell's refraction law:

$$n_t \sin\theta_t = n_i \sin\theta_i \tag{2.25}$$

where n_t and n_i are the refractive indices of the transmitted and incident material, respectively. In the case of $n_i > n_t$, θ_t is real only when θ_i is less than the critical angle given by.[37]:

$$\theta_c = \sin^{-1}\left(\frac{n_t}{n_i}\right) \tag{2.26}$$

Above this critical angle, there is no net transmission of energy; however, the boundary conditions require an electric field across the interface.[37] This field is referred to as the evanescent field, and as aforesaid; is used as the excitation source for TIR-Raman experiments. Figure 2.2 gives an example of the possible cases for an incident beam when $n_i > n_t$.

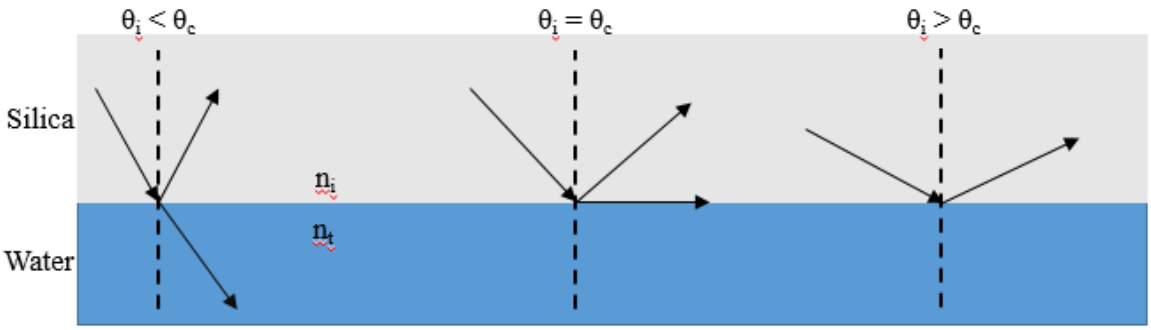

Figure 2.2: Examples of light incident below, at, and above the critical angle of the silica-aqueous interface. The refractive indices of silica and water at 532 nm are 1.461 and 1.336, respectively.

2.1.4 Evanescent Wave and Penetration Depth

As mentioned above, even with no transmission of energy across the interface; there is still an electric field at the interface, and it is referred to as an evanescent field. This field decays exponentially with distance (z) from the interface according to:[37]

$$E_t(z) = E_{0t}e^{-k_t\beta z} \tag{2.27}$$

with

$$k_t = \frac{2\pi n_t}{\lambda_0} \tag{2.28}$$

$$\beta = \sqrt{\left(\frac{n_i}{n_t}\right)^2 \sin^2\theta_i - 1} \tag{2.29}$$

where E_{0t} is the electric field of the "transmitted" light at the interface. The evanescent field decays with a length of:

$$L_d = \frac{1}{k_t\beta} \tag{2.30}$$

Because Raman scattering is proportional to the square of the excitation electric field, TIR-Raman probes a region adjacent to the interface with a thickness of:

$$D_p = \frac{1}{2k_t\beta} \tag{2.31}$$

Utilizing Eqn. (2.28), with 532.1 nm as the excitation wavelength, k_t was found to be 0.0158644 nm^{-1}. From Eqn. (2.29), with an incidence angle of 69.6°, and the indices of refraction of silica and a 1 M NaCl solution; β was calculated to be 0.197181628. With these values, Eqn. (2.31) was used to give a probing depth of 159.8 nm.

Below are the expressions for the complex transmission coefficients:[37]

$$t_{Px} = \frac{2\cos\theta_i(\sin^2\theta_i - n^2) + 2in^2\cos^2\theta_i\sqrt{\sin^2\theta_i - n^2}}{n^4\cos^2\theta_i + \sin^2\theta_i - n^2} \tag{2.32}$$

$$t_{Sy} = \frac{2\cos^2\theta_i - 2i\cos\theta_i\sqrt{\sin^2\theta_i - n^2}}{1 - n^2} \tag{2.33}$$

$$t_{Pz} = \frac{2n^2\cos^2\theta_i\sin\theta_i - 2i\cos\theta_i\sin\theta_i\sqrt{\sin^2\theta_i - n^2}}{n^4\cos^2\theta_i + \sin^2\theta_i - n^2} \tag{2.34}$$

where for simplicity $n = {}^{n_i}/_{n_t}$.

Figure 2.3 shows the absolute values of the transmission coefficients, the Frensel factors, for the case of a silica-aqueous interface.

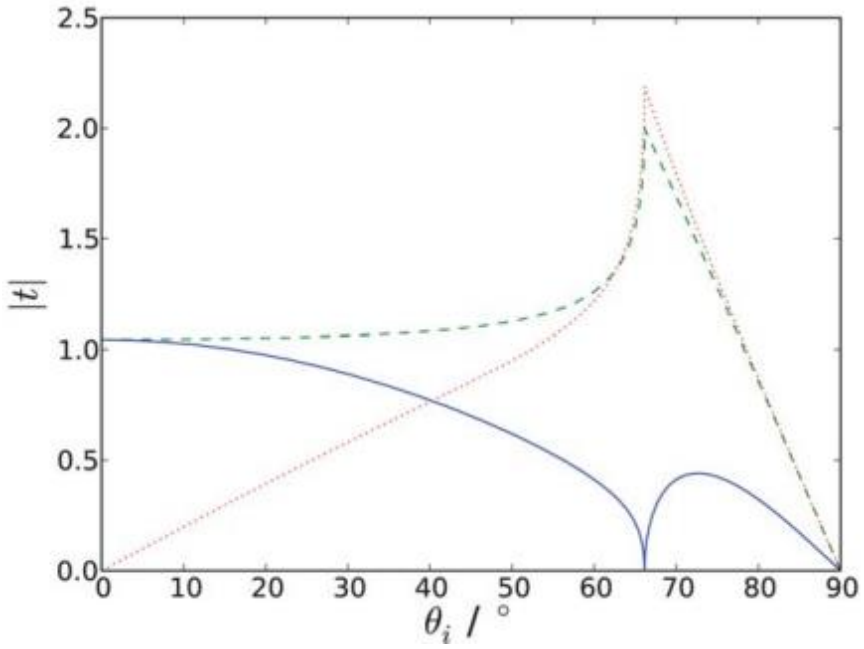

Figure 2.3: Absolute values of the Fresnel factors t_{Px} (solid blue line), t_{Sy} (dashed green line), and t_{Pz} (dotted red line) as a function of incident angle at the silica-aqueous interface This figure is reproduced from Ref. 3 with permission from The Royal Society of Chemistry (see Appendix A for copyright information).

Note that at the critical angle (66.1°), $|t_{Sy}|$ and $|t_{Pz}|$ are at their maximum, and $|t_{Px}|$ vanishes. This allows for the isolation of Raman scattering from only *z*-polarized incident light at the critical angle.

2.2 Group Theory and the Reduction of Symmetry Upon Adsorption

2.2.1 Basic Group Theory Background

Knowledge of the symmetry of a molecule can help immensely in the analysis of vibrational spectra. It is convenient to understand to which point group a molecule belongs, as information can be directly obtained from knowing this. At this stage, it is only

necessary to know that a Raman transition may occur when the polarizability of the molecule changes during a vibration. Consider a molecule with N atoms, there are $3N$ movements to consider as the atoms are displaced. For a non-linear molecule, there are three translations, and three rotations to consider, leaving $(3N - 6)$ vibrational modes. If a molecule is linear, three translations still exist, however rotation about the primary axis does not generate a displacement; as such, there are $(3N - 5)$ vibrational modes to consider. As an example, let us consider water, there are three atoms and it is non-linear, thus there are three vibrational modes for water. The vibrational modes for water are the symmetric stretch, antisymmetric stretch, and the bending mode (Figure 2.4).

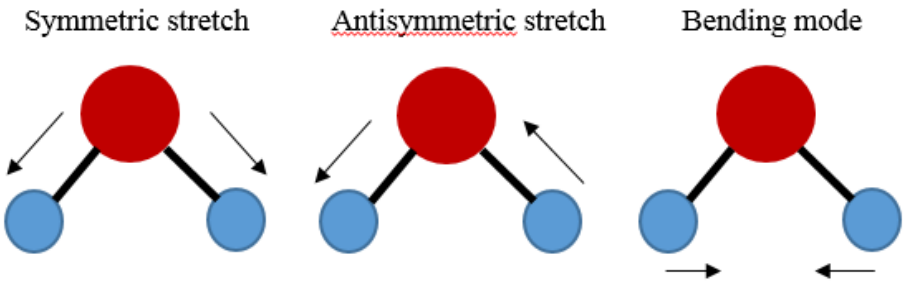

Figure 2.4: Vibrational modes of water.

To determine if a vibration is IR- or Raman-active, one must consider the selection rules for each case. For IR this is relatively easy as one would check to see if the dipole moment of a given molecule changes under a given vibration; for water, all three vibrational modes are IR-active. Determining Raman activity is not so intuitive however, as it is a bit more difficult to determine if the polarizability of a given molecule changes upon vibration. A good place to start looking would be vibrations that lead to a swelling

of a given molecule; such as the symmetric stretch of CO_2. One general rule that aids with this difficulty is the exclusion principle; if a given molecule has an -inversion center, none of its vibrations are both Raman- and IR-active.[38] At this point in time, it is enough to identify the point group to which a given molecule belongs and check the character table for that point group.

The character table for a given point group provides all of the symmetry elements with a description of how various objects transform under the corresponding operation. Table 2.1 gives the structure of a typical character table adapted from Ref. 13:

Table 2.1: Typical structure of a character table.

Name of point group	Symmetry operations arranged by class (E, C_n, etc.)	Functions	Further functions	Order of group
Symmetry species	Characters	Translations, rotations, and components of dipole for IR activity	Quadratic functions (x^2, xy, etc.) indicating Raman activity	

The main area is that of the characters, these show how an object, i.e., an atomic orbital, is affected by the corresponding symmetry operation. If the value is given as a "1" the orbital remains unchanged, "-1" means the sign is flipped, and "0" is indicative of a more complex change. The class of an operation is a grouping of similar operations, such as twofold rotations about different axis. If there are three similar operations, say twofold rotations, this would be listed as $3C_2$; all operations in the same class have the same

character.[38] The symmetry species acts as a label for each row describing the symmetry of that particular row. Each row is termed as an irreducible representation, basically the fundamental symmetry of in the group. The species label "A" means the function is symmetric (character = 1) with respect to the principle operation of the group; like the C_2 in the C_{2v} point group. The label "B" corresponds to a character of -1 for the principle operation. A subscript of "1" indicates a character of 1 for the principle reflection of the group; "2" means a character of -1. The order of the point group is simply the total number of symmetry operations which may be carried out for that point group. In the event of degenerate orbitals, the label "E" or "T" are used for double and triple degeneracy. The two columns listing functions simply give example functions; those defined by a single axis (x, y, z) or rotations (R_x, R_y, R_z) and those defined by multiple axes (i.e., x^2, xy, yz, $x^2 + y^2$). IR activity is described by functions dependent on one axis, Raman activity is described by multiple axis (quadratic) functions.[38]

2.2.2 Symmetry of Bulk Oxyanions and their Active Modes

Bulk selenate exists as a tetrahedral, which is very symmetric; so much that tetrahedral molecules have their own point group (T_d) and character table. Table 2.2 gives the character table for the T_d point group adapted from Ref. 13:

Table 2.2: Character table for T_d point group. Note there is only one quadratic equation associated to the totally symmetric representation, A_1.

T_d	E	$8C_3$	$3C_2$	$6S_4$	$6\sigma_d$	$h = 24$	
A_1	1	1	1	1	1		$x^2 + y^2 + z^2$
A_2	1	1	1	-1	-1		
E	2	-1	2	0	0		$(2z^2 - x^2 - y^2, x^2 - y^2)$
T_1	3	0	-1	1	-1	(R_x, R_y, R_z)	
T_2	3	0	-1	-1	1	(x, y, z)	(xy, yz, zx)

In Table 2.2 the species A_1 and the corresponding irreducible representation correspond to the symmetric stretch vibration. As the function listed is quadratic, and there is only one function, there is one peak for the symmetric stretching mode in the Raman spectrum of a tetrahedral molecule. Selenate for example has one symmetric stretch located at approximately 840 cm^{-1}.

2.2.3 Symmetry of Adsorbed Species and their Active Modes

Upon adsorption, the symmetry of a given molecule may change pending the type of adsorption the molecule undergoes. If a tetrahedral adsorbs in a monodentate fashion, they symmetry will be lowered from that of a T_d to a C_{3v}.[39] Upon adsorption in a bidentate fashion, the symmetry will become that of a C_{2v} point group. Tables 2.3 and 2.4 give the character tables for each of these point groups as adapted from Ref. 13.

Table 2.3: Character table for C_{3v} point group. Note the two quadratic equations associated with the totally symmetric representation A_1.

C_{3v}	E	$2C_3$	$3\sigma_v$		$h = 6$
A_1	1	1	1	z	$x^2 + y^2, z^2$
A_2	1	1	-1	R_z	
E	2	-1	0	(x, y) (R_x, R_y)	$(x^2 - y^2, xy)$ (zx, yz)

Table 2.4: Character table for C_{2v} point group. Note there are three quadratic equations associated with the totally symmetric representation.

C_{2v}	E	C_2	σ_v (xz)	σ'_v (yz)		$h = 4$
A_1	1	1	1	1	z	x^2, y^2, z^2
A_2	1	1	-1	-1	R_z	xy
B_1	1	-1	1	-1	x, R_y	zx
B_2	1	-1	-1	1	y, R_x	yz

From the above character tables it is clear that molecules belonging to the T_d point group have one peak for the symmetric stretch in a Raman spectrum; while C_{3v} and C_{2v} have two and three peaks in their Raman spectra respectively. It has been shown previously that adsorption of a tetrahedral oxyanion like sulfate in a monodentate fashion lowers its T_d symmetry to a C_{3v} symmetry, and bidentate lowers the symmetry further to a C_{2v} geometry.[39-40] As this is the case for any tetrahedral molecule, the same will follow for selenate. That is, if selenate adsorbs in a monodentate geometry, the symmetric stretch will be observed as two peaks in the Raman spectrum; and if a bidentate geometry is taken, the symmetric stretch will split into three peaks. Figure 2.5 shows a diagram illustrating the splitting of the single T_d symmetric stretch with the associated reduction of symmetry reminiscent of that used by Hug for the IR active modes of sulfate.[39]

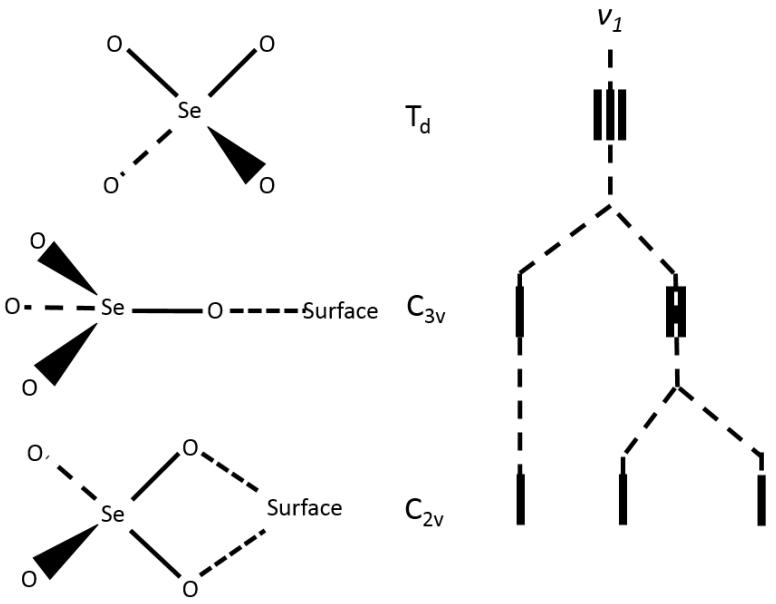

Figure 2.5: Diagram of the splitting of the symmetric stretch (ν_1) upon adsorption to a surface and subsequent lowering of symmetry from a T_d geometry to either C_{3v} or C_{2v}.

CHAPTER 3: MATERIALS AND METHODS

3.1 Materials

The sodium salts used in the selenite studies were: NaCl (Sigma-Aldrich, BioXtra ≥99.5%) and Na_2SeO_3 (Sigma-Aldrich, 99%). The other salts used during the "spot-check" tests were: Na_2SO_4 (Fisher Scientific, ACS Grade), Na_2SO_3 (Sigma-Aldrich, ACS Grade, 98+%), and Na_2SeO_4 (Sigma-Aldrich, >95%). The sodium salts used in the selenate study were: NaCl (Fisher-Scientific, ACS Grade, 99.5%), and Na_2SeO_4 (Acros-Organics, 98%). The chemicals used for cleaning the hemisphere were: H_2SO_4 (Fisher-Scientific, ACS Plus), $(NH_4)_2S_2O_8$ (Fisher-Scientific, ACS Grade, 99.3%), Methanol (Acros-Organics, Spectroscopy Grade, 99.9%). The HCl and NaOH used for pH adjustment were: HCl (Fisher-Scientific, trace-metal grade), NaOH (Mallinckrodt, 99%) The fused silica hemispheres were purchased from ISP Optics and cleaned as described below (part no. QU-HS-25). The surface quality of the hemisphere was 60/40 with a tolerance of 0.01 mm on diameter and 0.05 mm on thickness.

All glassware was thoroughly cleaned before use utilizing a mixture of H_2SO_4 and $(NH_4)_2S_2O_8$. For every 500 mL of acid, approximately 8 g of the oxidant was added; the glassware was allowed to soak for 3-4 h, then rinsed copiously with nanopure water. The quartz cuvettes were cleaned using a dilution of Hellmanex II detergent (Hellma, Item no. 9-307-010-507). The cuvettes were allowed to soak for 2-3 h, then rinsed copiously with

nanopure water. Polishing of the silica hemispheres was done by using a Buehler microcloth (part no. 40-7218) and a 0.05 µm colloidal suspension of alumina (MasterPrep Polishing Suspension, Buehler, part no. 40-6377-032). This was performed by pouring a small amount of the suspension onto the microcloth and, making small circles, polishing the flat side of the hemispheres. They were then rinsed copiously with nanopure water. This was repeated until the hemispheres were clear.

3.2 Solution Preparation

All solutions were prepared using ultrapure water with a resistance of 18.1-18.3 MΩ·cm from a Barnstead Nanopure system (Model #: D4741, Company: Thermolyne) with two extra organic removal cartridges (Part #: D5026 Type I Organic Free Cartridge Kit). For the selenite studies, five concentrations were used (50, 100, 150, 200, and 250 mM), and two pHs were tested (pH 6 and 7). The ten solutions were also made with 1 M NaCl to act as a background electrolyte. This was done by preparing a mother solution that was 1 M in both Na_2SeO_3 and NaCl, then diluting that with a 1 M NaCl solution to obtain appropriate concentrations of Na_2SeO_3. These solutions were stored in 500 mL Fisher-brand Kimax storage bottles (item no. FB-800-500). The "spot check" solution concentrations were 250 mM for each salt, the pH was not adjusted for these solutions.

The solutions used for the selenate studies were prepared in the same fashion, and stored similarly. Five concentrations were also used for these, however to aid in detection the range was shifted to 150-350 mM in increments of 50 mM. These solutions were

adjusted to be pH of 5, 6, and 7 using the name NaOH and HCl as mentioned above. These five solutions were also made with 1 M NaCl as a background electrolyte.

The pH meter used for adjustment was an Accumet Basic AB15 pH meter with an Accumet TRIS Compatible Combination pH Electrode. The standard pH 4, 7, and 10 buffers used were from Fisher-scientific and adjusted for a 1 M NaCl background electrolyte by addition of 0.1 mol NaCl to 100 mL of the solutions. These stock solutions were kept for repeated use. A speciation curve for aqueous selenate and selenite is given in Figure 3.2; note that for the pH range tested, selenate exists almost completely as the fully non-protonated form SeO_4^{2-}.

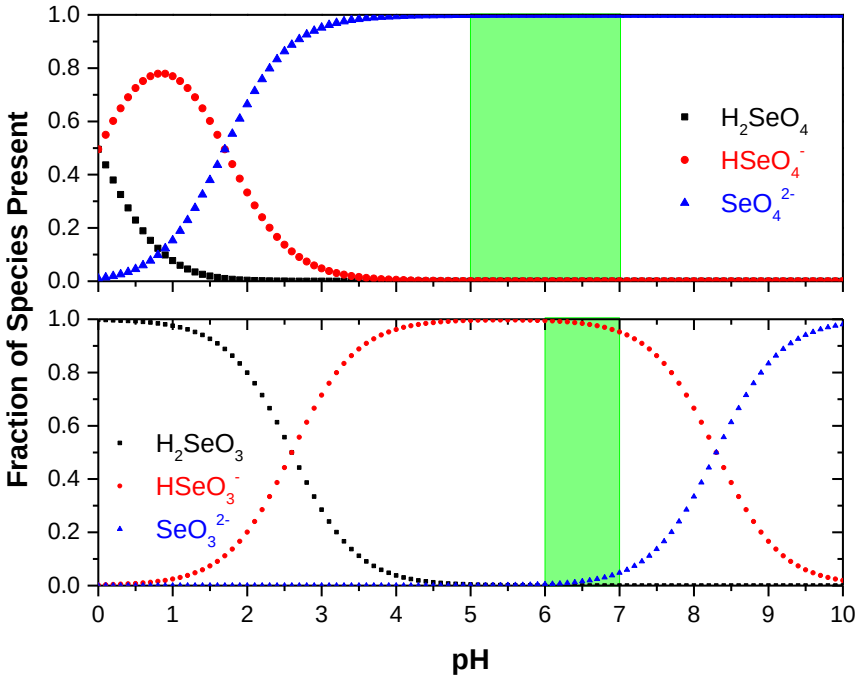

Figure 3.1: Speciation curve for aqueous selenate and selenite. The green areas highlight the range covered by the prepared solutions. Note that at pH > 5, $[SeO_4^{2-}] > 99\% [Se]_{tot}$.

3.3 Conventional Raman Set-up

For the conventional Raman studies, a system was custom-built. The laser used for excitation was a continuous wave, single-mode (TEM_{00}) 532.1 nm Nd:YVO_4 laser (Millenium II, Spectra-Physics). This laser was coupled into a 5 mm focusing Inphotonics Raman probe (Model no. RPS532/12-10). The laser was operating with an output of approximately 880 mW, while the output of the probe was approximately 50 mW. This output was focused into a Thorlabs quartz cuvette with four polished windows that was used for the sample cell (part no. CV10Q3500F-E). Raman scattering was collected at 90° from excitation, and focused through a 532 nm RazorEdge ultrasteep long-pass edge filter (Semrock, part no. LP03-532RE-25) into a Princeton Instruments SpectraPro 500i monochromator utilizing a 1200 groove/mm grating and a slit width of 100 μm. This was coupled to a liquid nitrogen-cooled deep-depletion CCD (1340/400 EB, Roper Scientific). The monochromator and CCD were calibrated against the 435.833 nm line of an Hg vapor lamp. The software used was SpectraSense 5.0.0 from Princeton Instruments. Spectra were obtained with a 120 s exposure time utilizing the cosmic correction function. Each spectrum is the average of three taken consecutively. The spectra cover the range from 75-1200 cm^{-1}. Photographs of the set-up are given in Figures 3.2-3.4. Fig. 3.2 presents overview to show the relative positions of the optical components from the TIR studies to be discussed. Figs. 3.3 and 3.4 give more details and an outline of the beam path for the experiment. The neutral density filter (NDF) was not mentioned above as it was set to allow 100% transmittance.

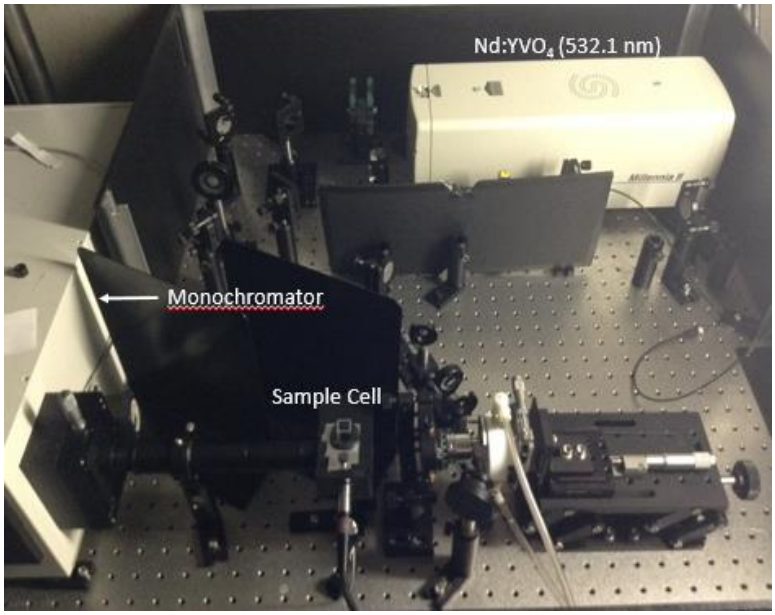

Figure 3.2: Overview of the setup used for conventional Raman experiments.

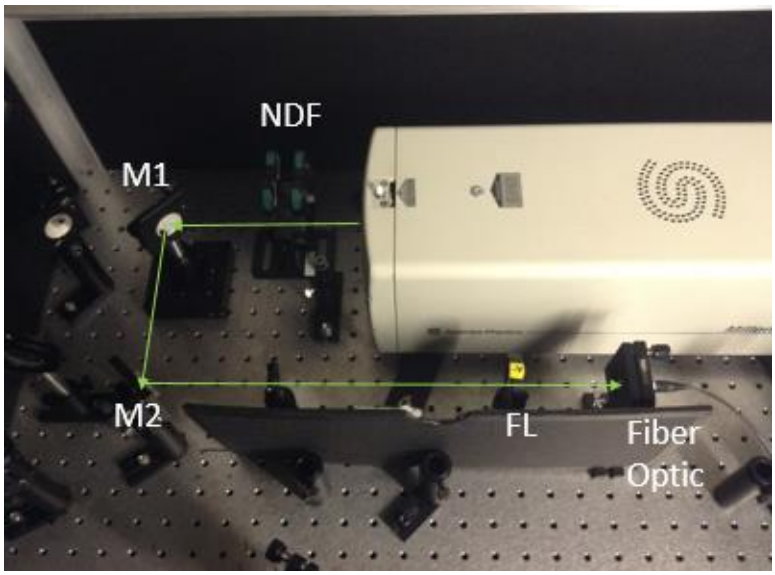

Figure 3.3: First half of the beam path for the conventional Raman experiments. The neutral density filter (NDF) wheel is set to allow 100% transmittance. Mirrors (M1 and M2) and input focusing lens (75 mm, FL) are also shown.

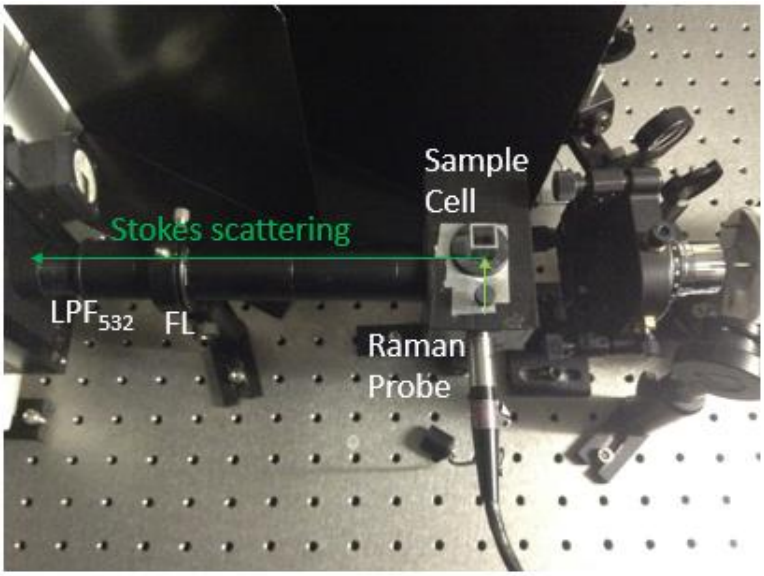

Figure 3.4: Second half of the beam path for the conventional Raman experiments. The output focusing lens (70 mm, FL) and 532 nm long pass filter (LPF_{532}) are shown.

3.4 TIR-Raman Setup

The TIR-Raman setup used was also custom-built. This setup utilized the same laser as mentioned above. The laser output was approximately 220 mW initially, and tuned down to approximately 45 mW by directing the beam through the NDF filter wheel. After this, the beam was turned 180° with two mirrors, and directed to a third mirror. After reflection from the third mirror, another was used to direct the beam through a focusing lens into the silica hemisphere. Raman scattering was collected via a Nikon 50× objective lens (infinity-corrected, super-long working distance (13.8 mm), 0.45 numerical aperture) which was mounted normal to the silica hemisphere. The objective was mounted on a 6-axis kinematic optic mount (Thorlabs, Part no. K6XS) for ease of alignment and to increase

efficiency of the collection of scattering. The scattering was focused through the same focusing lens and filter into the same monochromator used in the conventional setup. The monochromator was set to use the same grating as above, which was also calibrated with the 435.833 nm line of an Hg arc lamp. The same deep-depletion CCD was used to collect the spectra, which was viewed in the SpectraSense software. The spectra were collected with a 180 s exposure time making use of cosmic correction over the range 650-1200 cm^{-1}. Due to a quirk within the workings of SpectraSense, although the range was set as mentioned, the actual spectra covered the range 550-1200 cm^{-1}. The photograph in Figure 3.5 is shown to give a clearer understanding of the setup used for TIR-Raman experiments. The incidence angle of this system was determined by placing posts in corresponding locations around the cell and last mirror allowing for strings to be tied to them and a right triangle formed. The sides of this triangle were measured and Pythagoras' theorem was used to calculate the incidence angle. The incident angle was determined to be 69.6°. Figure 3.6 is a picture that was taken during the determination of the incidence angle to clarify the method described above.

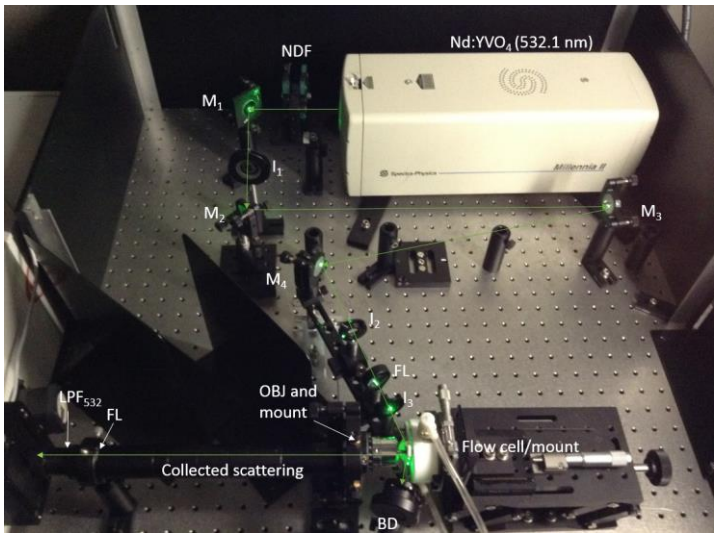

Figure 3.5: Image detailing the TIR-Raman setup and beam path. The following optical components are shown: neutral density filter (NDF), mirrors (M), irises (I), focusing lenses (Fl), microscope objective (OBJ), beam dump (BD), and 532 nm long pass filter (LPF_{532}).

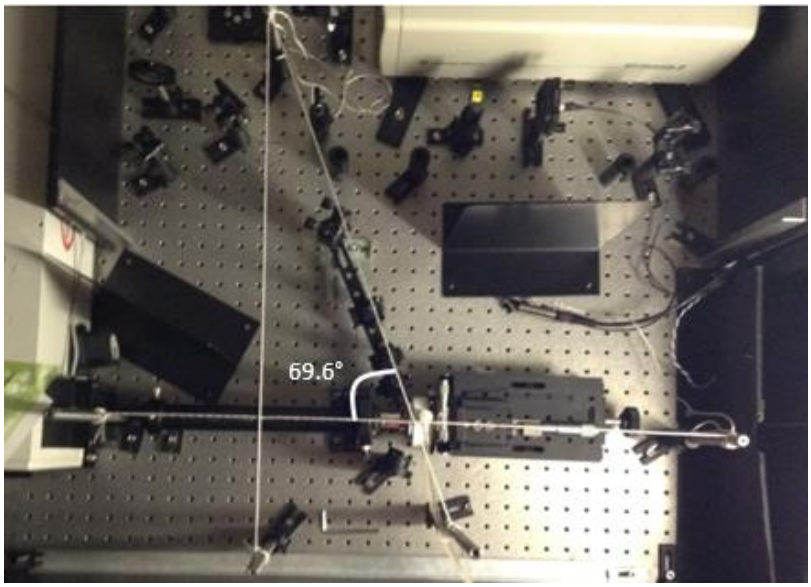

Figure 3.6: Photograph depicting the determination of the incident angle of the TIR-Raman system utilized herein. The incident angle was determined to be 69.6°.

3.5 Data Processing and Fitting

Raw spectra were initially analyzed within SpectraSense by subtracting a background spectrum. This background was a spectrum of just a 1 M NaCl solution that was adjusted to the appropriate pH. These background-subtracted spectra were then converted to a .txt file and imported into OriginPro version 9.0.1. Origin was used to plot the spectra and used to fit the spectra utilizing the Multiple Peak Fit tool. Spectra were fit utilizing a Voigt fitting function for each peak. The data was fit over the range of 600-1200 cm^{-1}. For the conventional data, only the symmetric and anti-symmetric peaks were fitted, because the two bending modes were not included in TIR-Raman spectra as they overlap with a very intense silica mode that would flood the camera unless shorter exposure times were used. For TIR-Raman, an initial attempt was made to fit the symmetric and antisymmetric stretch for each spectrum; whether or not both peaks were fit, or only the symmetric stretch, depended on the individual spectrum. Origin was then used to construct the various plots shown using data from the fitting that was performed. Figure 3.7 outlines the spectral processing and fitting procedure using the TIR-Raman data for the pH 6, 350 mM Na_2SeO_4 solution.

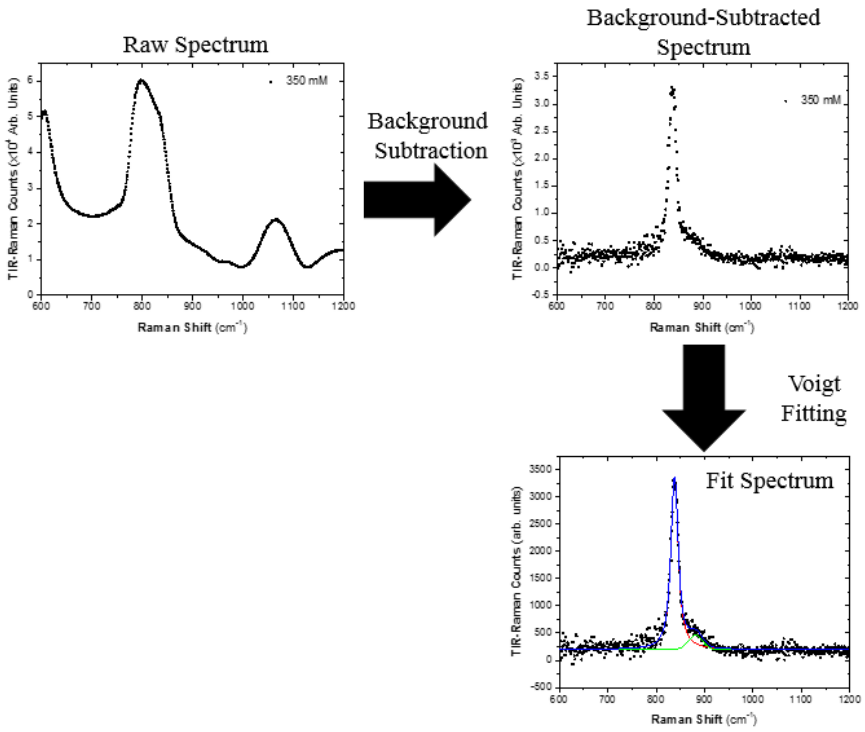

Figure 3.7: Flow chart outlining the data processing and fitting procedure.

CHAPTER 4: RESULTS AND DISCUSSION

4.1 Selenate

4.1.1. Bulk Raman Spectra of Selenate Solutions

The Raman spectrum of a 1 M NaCl solution was collected and used as a background. This spectrum along with the spectra of the three pH 6 Na_2SeO_4 solutions are shown in Figure 4.1.

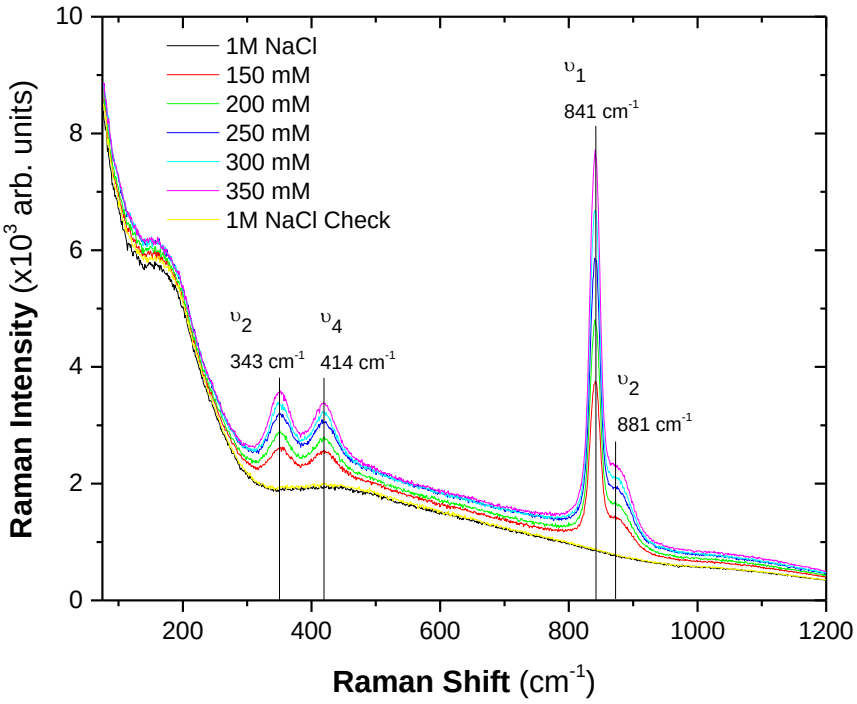

Figure 4.1: Raw Raman spectra of a pH 6, 1 M NaCl solution and five Na_2SeO_4 solutions of varying concentration and also with 1 M NaCl.

The large feature at ~180 cm^{-1} is likely an artifact or possibly a water mode. Note that it has the same intensity in the selenate and NaCl solution spectra. Background-subtracted spectra of the pH 6 Na_2SeO_4 solutions are shown in Figure 4.2.

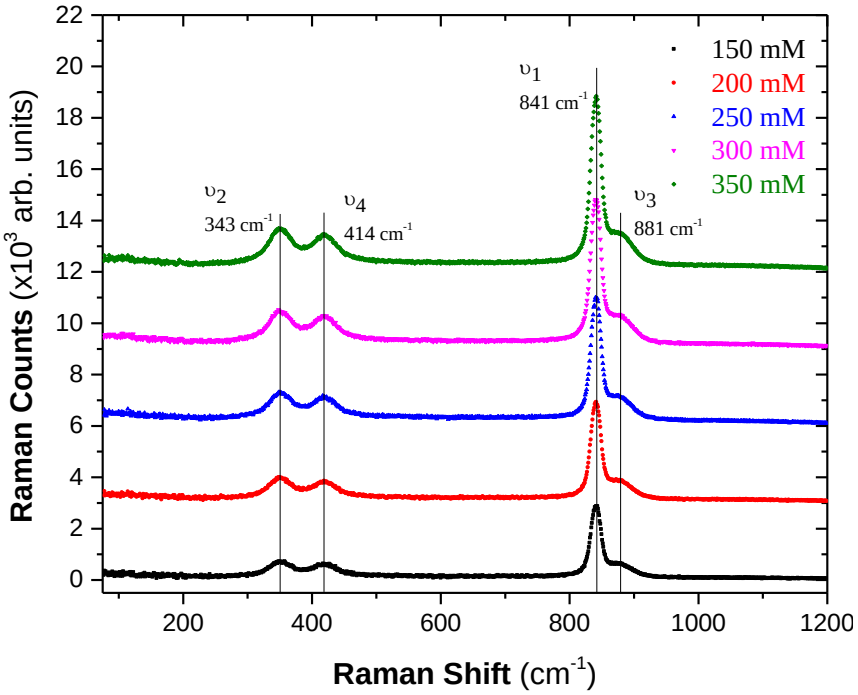

Figure 4.2: Background-subtracted pH 6 Raman spectra of Na_2SeO_4 solutions.

The main feature of the selenate spectrum is the large peak at ~841 cm^{-1}. This peak is from the υ_1 of the tetrahedral structure.[42-43] This corresponds to the symmetric stretching motion of the anion.[44] The shoulder located at ~881 cm^{-1} is attributed to the antisymmetric stretching υ_3 mode.[42-44] The two smaller peaks at ~343 and ~414 cm^{-1} are both attributed to the υ_2 and υ_4 bending modes, respectively.[42-44] Table 4.1 below gives a quick summary of these assignments. Note the disappearance of the large feature at ~180 cm^{-1}; this

background subtraction thus shows that it is not a feature that can be attributed to the tetrahedral selenate anion. There is also an almost linear increase with intensity that can be seen, which is to be expected for bulk Raman studies. The spectra of the pH 5 and 7 solution sets are reported in Figures 4.3 and 4.4. They match very well with the pH 6 spectra (Figure 4.2).

Table 4.1: Peak assignments of aqueous Na_2SeO_4 bulk Raman spectra.

Peak Frequency (cm^{-1})	Assignment	Description	Mode
~343	υ_2	Deformation	Bending
~414	υ_4	Deformation	Bending
~840	υ_1	Valence vibration	Symmetric stretch
~880	υ_3	Valence vibration	Asymmetric stretch

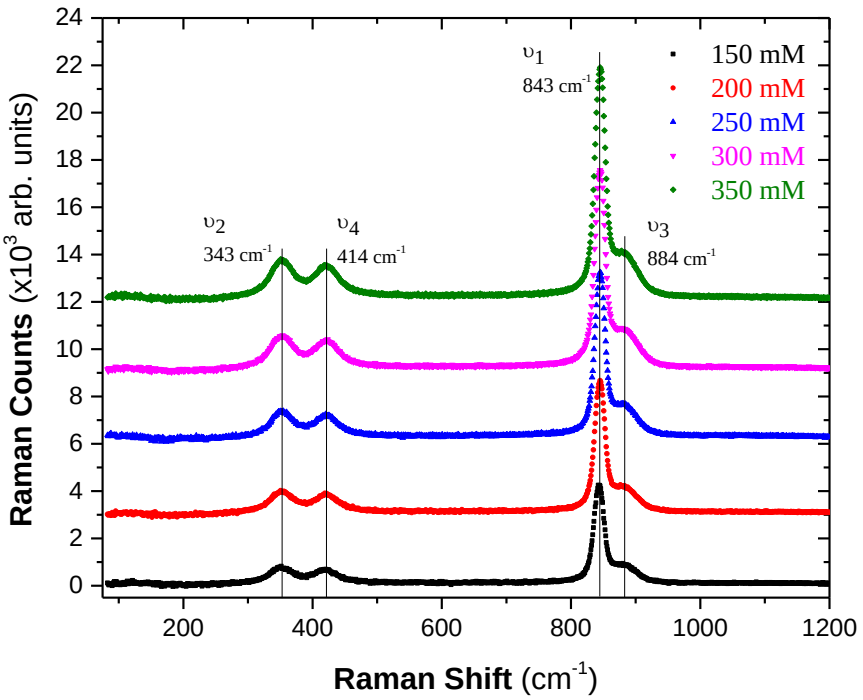

Figure 4.3: Background-subtracted bulk Raman spectra of pH 5 Na_2SeO_4 solutions.

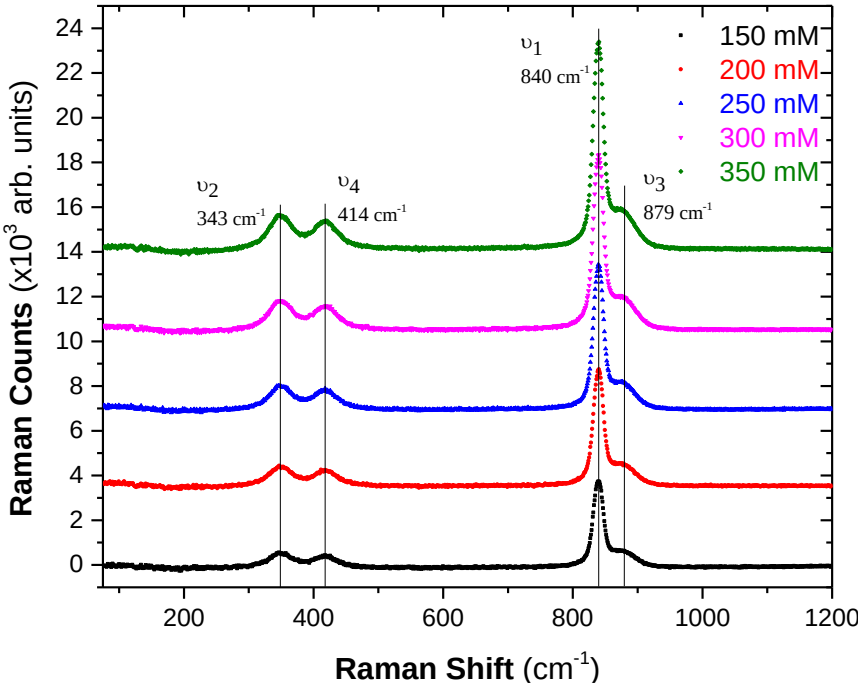

Figure 4.4: Background-subtracted bulk Raman spectra of pH 7 Na_2SeO_4 solutions.

Considering that the symmetric stretching region is the real region of interest, the spectra were then fit over the region 600–1200 cm^{-1}. The fit was done utilizing two Voigt functions, one to fit the symmetric stretch, and one for the antisymmetric stretch. This fitting was done for each of the 15 background-subtracted spectra. Figure 4.5 below shows the fitting for the pH 5 150 mM Na_2SeO_4 spectrum.

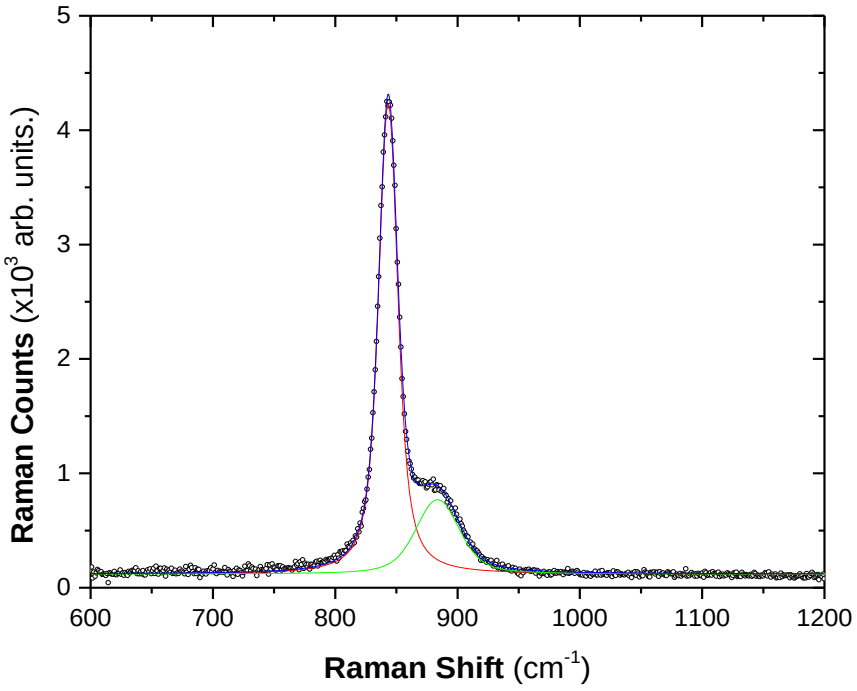

Figure 4.5: Fitting for the pH 5 150 mM Na_2SeO_4 spectrum over the region 600–1200 cm^{-1}. The fits to the symmetric (red) and antisymmetric (green) stretches as well as the cumulative fit (blue) are shown.

For all fits, a goodness of fit (R^2) > 0.99 was obtained; and other fitting parameters obtained include; the *y*-intercept (y_0) of each curve, the center frequency for each peak (ω_0), the full width at half maximum (FWHM), the peak area, and the Gaussian and Lorentzian widths (W_g and W_l). Tables 4.2 and 4.3 list these fitting parameters obtained for the symmetric and antisymmetric stretches respectively; the values in parenthesis are the fit errors. Note that R^2 and y_0 values are the same for each peak in the tables as those two parameters refer to the cumulative fit, not the individual peaks.

Table 4.2: Voigt fitting parameters (with fit errors) for the symmetric stretch from the conventional data.

C	y_0	ω_0 (cm^{-1})	FWHM (cm^{-1})	Area	W_g (cm^{-1})	W_l (cm^{-1})	R^2
			pH 5				
150	119 (1)	843.33 (0.03)	18.81 (0.07)	105800 (700)	11.2 (0.2)	11.8 (0.2)	0.99849
200	133 (2)	844.66 (0.02)	18.88 (0.06)	139000 (800)	11.8 (0.2)	11.2 (0.2)	0.99879
250	327 (2)	844.81 (0.02)	18.80 (0.05)	174000 (900)	11.7 (0.2)	11.2 (0.2)	0.99901
300	269 (2)	844.82 (0.02)	18.83 (0.06)	211000 (1000)	11.6 (0.2)	11.4 (0.2)	0.99893
350	231 (3)	844.86 (0.02)	18.92 (0.06)	245000 (1000)	11.8 (0.2)	11.3 (0.2)	0.99871
			pH 6				
150	106 (2)	840.81 (0.05)	19.1 (0.1)	72800 (900)	11.4 (0.4)	12.0 (0.4)	0.99443
200	155 (2)	840.73 (0.05)	19.0 (0.1)	97000 (1000)	11.6 (0.4)	11.7 (0.4)	0.99470
250	233 (4)	840.80 (0.06)	19.0 (0.2)	126000 (2000)	10.6 (0.5)	12.7 (0.5)	0.99153
300	238 (4)	840.59 (0.05)	19.0 (0.1)	146000 (2000)	11.3 (0.4)	12.1 (0.4)	0.99442
350	279 (4)	840.75 (0.04)	19.1 (0.1)	172000 (2000)	11.2 (0.4)	12.3 (0.4)	0.99556
			pH 7				
150	-92 (1)	839.30 (0.03)	18.58 (0.07)	94000 (700)	12.4 (0.2)	10.0 (0.2)	0.99809
200	34 (1)	839.50 (0.02)	18.63 (0.06)	127700 (700)	12.1 (0.2)	10.5 (0.2)	0.99890
250	-46 (2)	839.41 (0.02)	18.60 (0.05)	160400 (800)	11.8 (0.2)	10.7 (0.2)	0.99916
300	38 (2)	839.31 (0.02)	18.61 (0.05)	193000 (1000)	11.9 (0.2)	10.7 (0.2)	0.99915
350	139 (2)	839.01 (0.02)	18.63 (0.05)	229000 (1000)	11.9 (0.2)	10.7 (0.2)	0.99914

Table 4.3: Voigt fitting parameters (with fit errors) for the antisymmetric stretch from the conventional data.

C	y_0	ω_0 (cm^{-1})	FWHM (cm^{-1})	Area	W_g (cm^{-1})	W_l (cm^{-1})	R^2
				pH 5			
150	119 (2)	883.7 (0.3)	42.2 (0.7)	34600 (1000)	32 (2)	18 (2)	0.99849
200	133 (2)	884.6 (0.2)	42.0 (0.7)	50000 (1000)	28 (2)	23 (2)	0.99879
250	327 (2)	884.7 (0.2)	42.8 (0.6)	64000 (1000)	28 (2)	23 (2)	0.99901
300	269 (2)	885.1 (0.2)	42.8 (0.6)	73000 (2000)	31 (2)	20 (2)	0.99893
350	231 (3)	885.0 (0.2)	42.5 (0.7)	84000 (2000)	31 (2)	20 (2)	0.99871
				pH 6			
150	106 (2)	880.5 (0.5)	40 (1)	22000 (1000)	28 (3)	20 (4)	0.99443
200	155 (2)	880.2 (0.5)	40 (1)	31000 (2000)	28 (3)	20 (4)	0.99470
250	233 (4)	880.8 (0.6)	39 (2)	37000 (3000)	28 (4)	19 (5)	0.99153
300	238 (4)	880.3 (0.5)	41 (1)	46000 (3000)	29 (3)	20 (4)	0.99442
350	279 (4)	881.0 (0.4)	40 (1)	52000 (3000)	29 (3)	18 (4)	0.99556
				pH 7			
150	-92 (1)	878.4 (0.3)	43.1 (0.8)	31000 (1000)	38 (2)	9 (3)	0.99809
200	34 (1)	878.7 (0.2)	42.5 (0.6)	44000 (1000)	33 (1)	17 (2)	0.99890
250	-46 (2)	878.9 (0.2)	41.8 (0.5)	51000 (1000)	35 (1)	13 (2)	0.99916
300	38 (2)	878.6 (0.2)	42.3 (0.6)	64000 (1000)	33 (1)	16 (2)	0.99915
350	139 (2)	878.3 (0.2)	42.5 (0.6)	78000 (2000)	32 (1)	17 (2)	0.99914

From the above tables; it may be gleaned that with increasing concentration, the peak area for each curve increases linearly. To illustrate this point, Figures 4.6 and 4.7 were constructed to show the linearity of the peak area versus concentration for each of the symmetric and antisymmetric stretches, respectively.

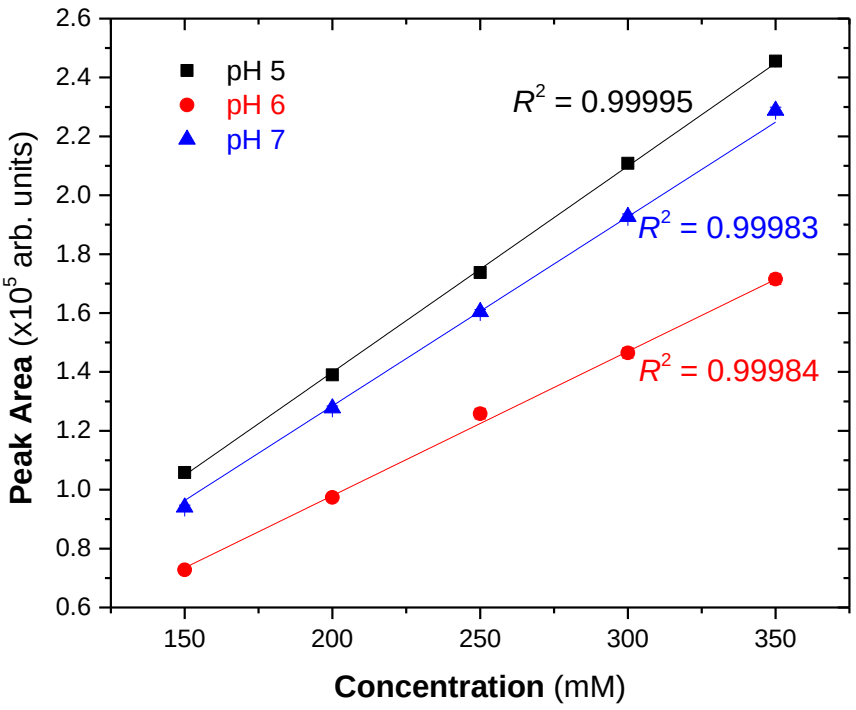

Figure 4.6: Peak area of the symmetric stretch vs. concentration for the three solution sets. The data was linearly fit, setting $y_0 = 0$.

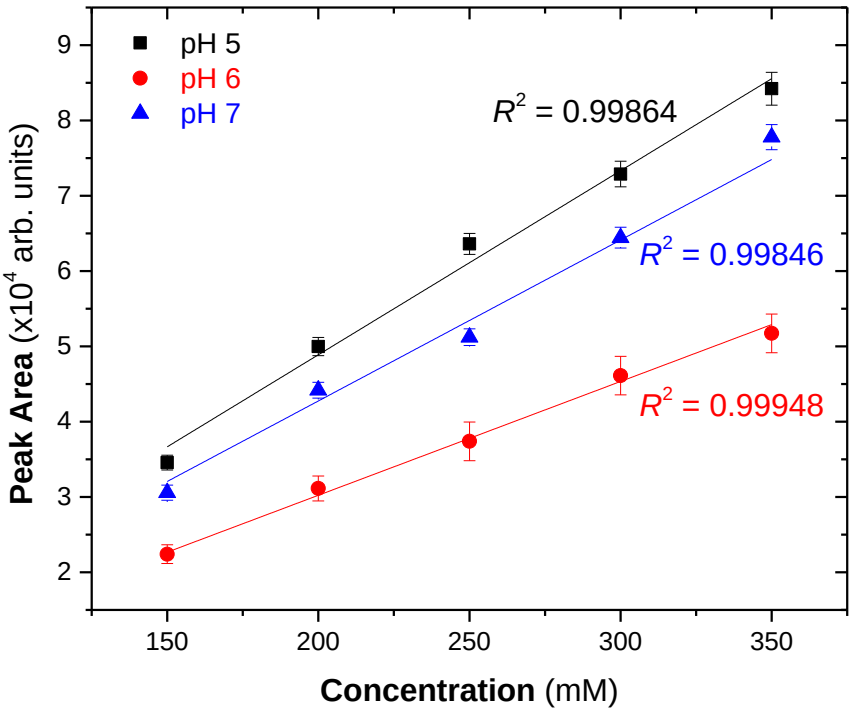

Figure 4.7: Peak area of the antisymmetric stretch vs. concentration for the three solution sets. Again, the data was linearly fit, setting $y_0 = 0$.

From Figures 4.6 and 4.7, it is obvious that the peak area for both stretches scales linearly with concentration. The error bars for the symmetric stretch plot are present, however they are difficult to see as the error here is <1%. For the antisymmetric stretch, the error bars are more evident as they represent up to 8%. As the antisymmetric stretch is much smaller than the symmetric stretch and overlaps with it as well; an accurate fit is more difficult to obtain for the antisymmetric stretch. Also, purely due the smaller peak area, an error value similar to that for the symmetric stretch errors will become more noticeable. An $R^2 > 0.998$ for all six fits supports the appropriate fitting obtained from linear fits with $y_0 = 0$. Forcing this intercept is valid as the fitting was done for spectra that

have already been background corrected, therefore; if the concentration of selenate is zero, there should be zero intensity for the associated peaks.

Another interesting plot that may be constructed from the above tables is that of the center frequency versus concentration for each solution set. As above, the two plots (Figures 4.8 and 4.9) represent the symmetric and antisymmetric stretches, respectively.

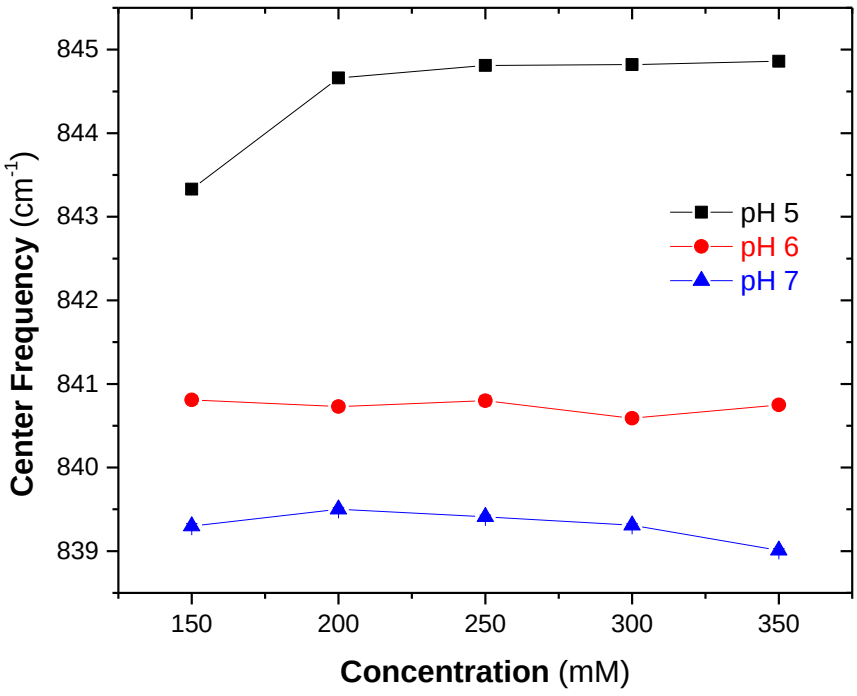

Figure 4.8: Center frequency of the symmetric stretch vs. concentration for each pH.

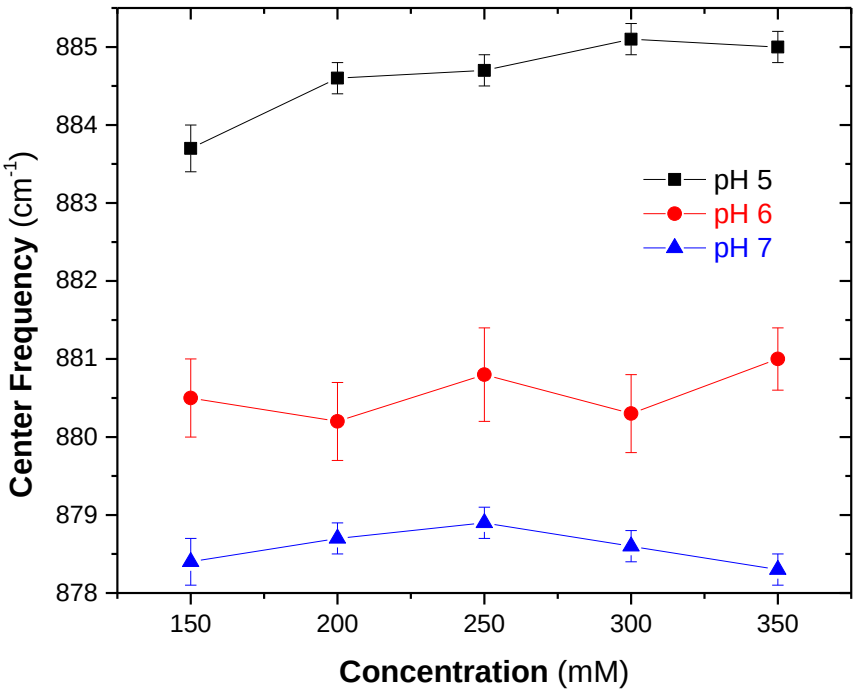

Figure 4.9: Center frequency of the antisymmetric stretch vs. concentration for each pH.

From the graphs one finds that within each solution set, the peak position is relatively constant for both the symmetric and antisymmetric stretches. The error bars for the symmetric stretch plots are present, but as above are so small they are difficult to see. The error bars for this peak are on the order of 0.05 cm^{-1}, very small compared to the scale of the graph. The error bars for the antisymmetric stretch are approximately one order of magnitude larger than those for the symmetric stretch. This is likely due to the antisymmetric stretch appearing as a "shoulder" on the right side of the symmetric stretch, and its relative size. Being smaller, and not nearly as defined as the symmetric stretch, an accurate fit is more difficult to obtain, and precision suffers. However, these errors are quite small as the data within each solution set varies only slightly with the largest shift

with increasing concentration is approximately 1.5 cm^{-1}. At this point one may notice that there appears to be a trend; with increasing pH, there is a red-shift of the peak positions. Plots of this trend were also constructed and are shown below in the same fashion as those above (Figures 4.10 and 4.11).

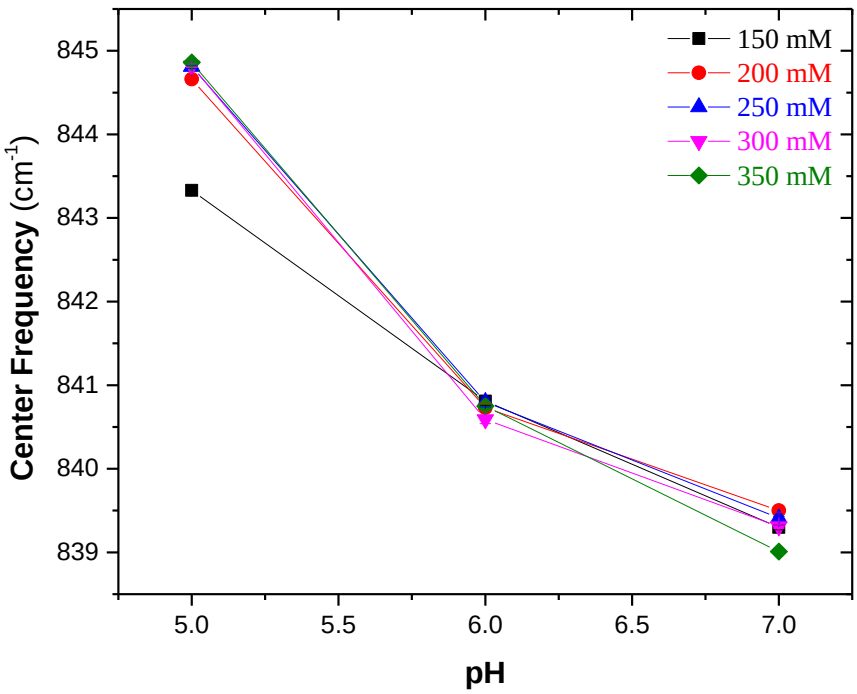

Figure 4.10: Center frequency of the symmetric stretch vs. pH for each concentration.

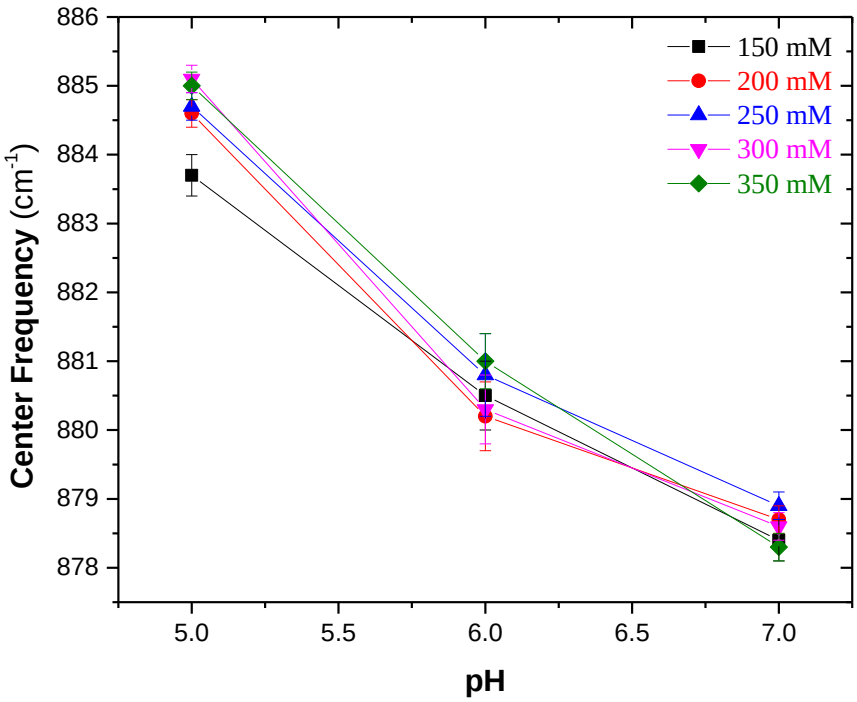

Figure 4.11: Center frequency of the antisymmetric stretch vs. pH for each concentration.

The above plots help to highlight the apparent red-shift with increasing pH for the solution sets. The error bars for these two plots are the same as those for the previous center frequency plots. At this point, this trend has not been duplicated, a repeat of these spectra will need to be performed to determine if this is something real, or a product of some error made in conducting the experiment. It is likely that this trend is meaningless as the overall shift is only on the order of 5 cm^{-1}, quite small to be an appreciable red-shift, and within the error of this setup; however, as aforesaid, further testing is required to check this.

4.1.2. TIR-Raman Spectra of Selenate Solutions on Silica

Figure 4.12 shows the raw spectra that were obtained for TIR-Raman of Na_2SeO_4 solutions on a silica surface. The shown spectra include all five concentrations, plus the background NaCl solution spectrum used for background subtraction for the pH 7 solution set.

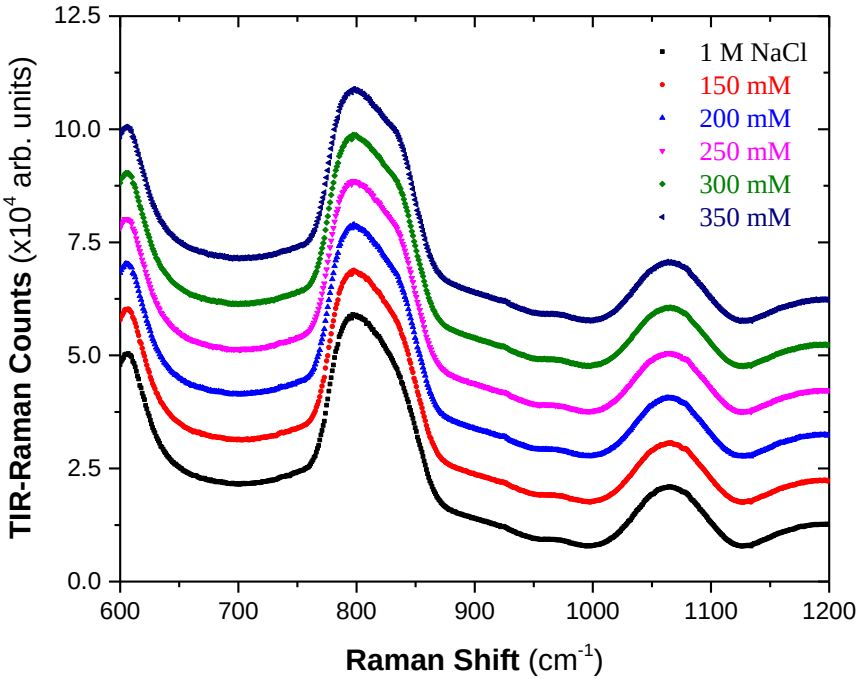

Figure 4.12: Raw TIR-Raman spectra of the pH 7 Na_2SeO_4 solutions.The spectra are stacked for clarity.

The large mode at 800 cm^{-1} is one of the silica modes, and lies on-top of the symmetric and antisymmetric stretching modes of selenate. Because of this, it is very difficult to see the selenate modes until a background subtraction is performed. This large mode also hinders acquisition times, as once it reaches 65,000 counts, the camera will be

flooded. This large mode is certainly an important limiting factor impacting the quality of spectra. In Figure 4.13, the background-subtracted pH 7 spectra are shown, again, stacked for clarity.

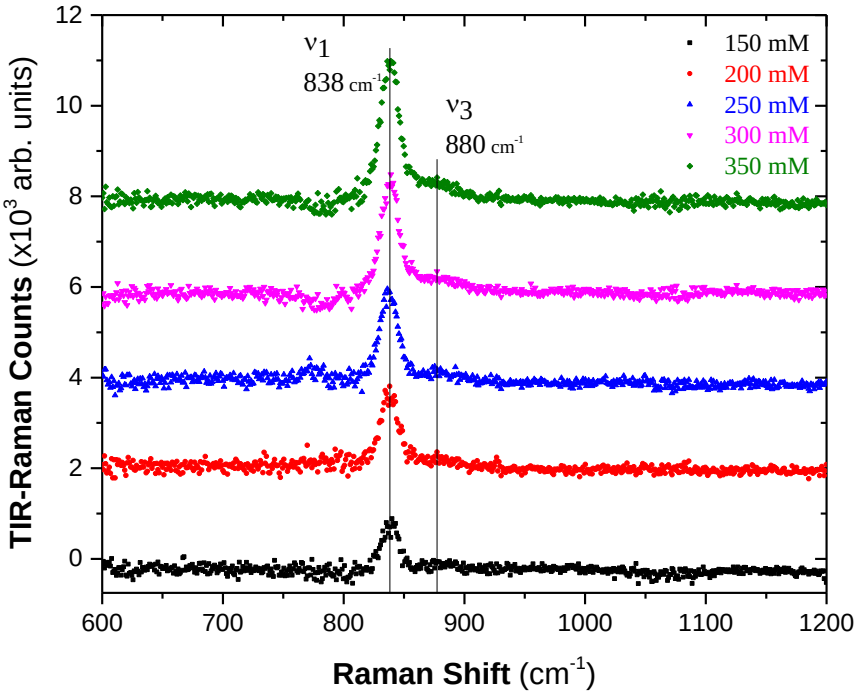

Figure 4.13: Background-subtracted TIR-Raman spectra of the pH 7 Na_2SeO_4 solutions. The spectra are stacked for clarity.

The above spectra show one large peak centered around 838 cm^{-1}, this peak is associated with the symmetric stretching mode of selenate as in the conventional spectra above. There is also a small peak around 880 cm^{-1} which, as before, corresponds to the anti-symmetric stretch. This peak is difficult to see here, but becomes more obvious when the spectra are plotted individually for fitting. The same spectra are shown below in

Figures 4.14 and 4.15 for the pH 5 and 6 solutions, respectively; the same modes can be seen as shown in Figure 4.13.

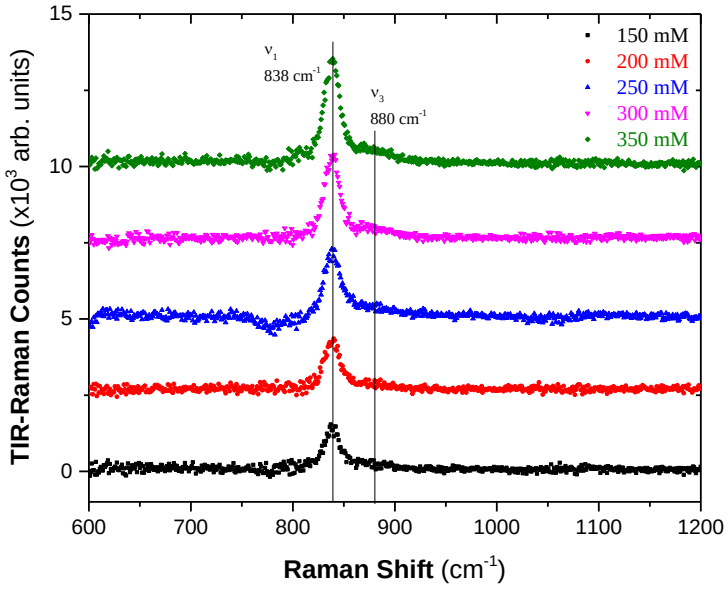

Figure 4.14: Background-subtracted TIR-Raman spectra of the pH 5 Na_2SeO_4 solutions. The spectra are stacked for clarity.

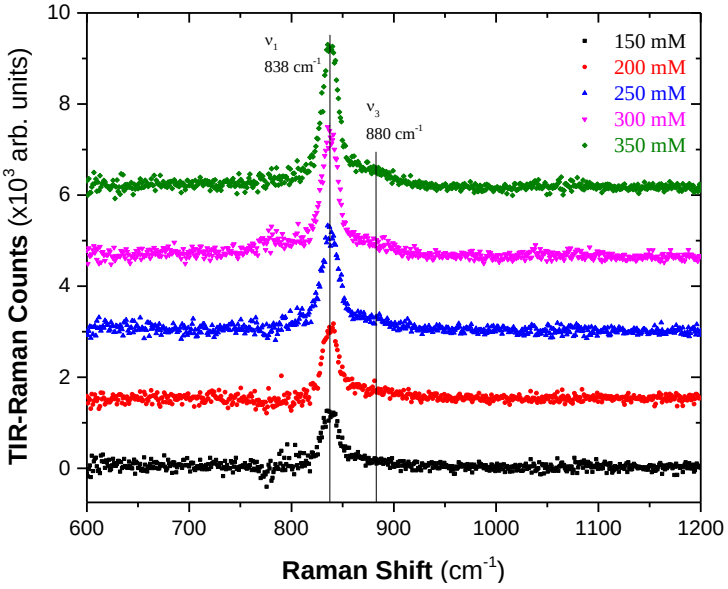

Figure 4.15: Background-subtracted TIR-Raman spectra of the pH 6 Na_2SeO_4 solutions. The spectra are stacked for clarity.

These spectra were then given the same treatment as was the conventional data in that they were individually plotted and fitted with Voigt curves. As the antisymmetric peak is of little importance to determine sorption, and for ease of fitting, the center frequency was set to be equal to the corresponding center frequency obtained from the conventional fits. In one spectrum, 150 mM pH 7, only one peak was used, as a fit for a second peak corresponding to the antisymmetric stretch was not obtainable. Figure 4.16 below shows an example of the obtained fits for one of the cleaner spectra, the pH 7 350 mM spectrum.

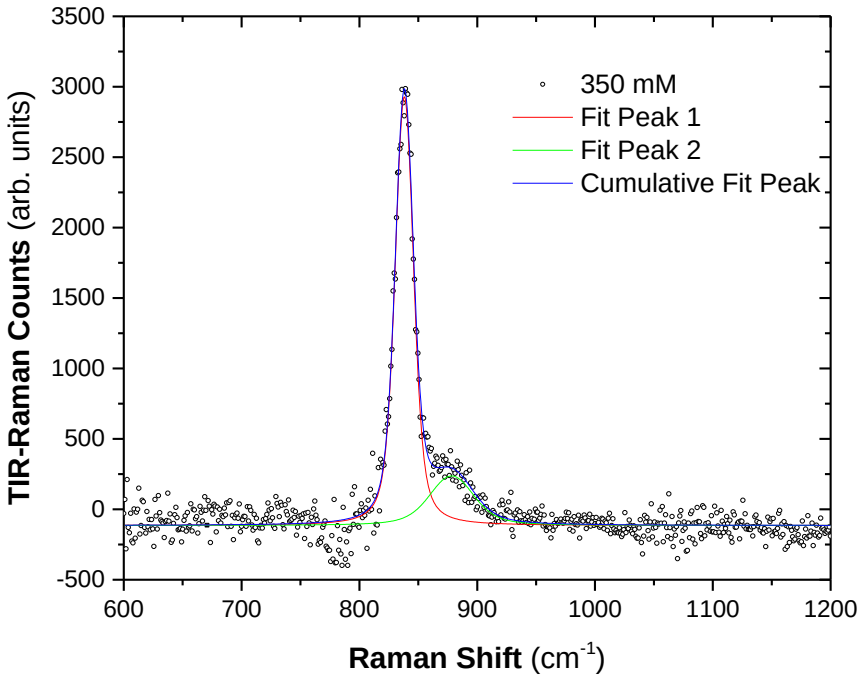

Figure 4.16: Fitting for the pH 7 350 mM Na_2SeO_4 solution spectrum over the region 600–1200 cm^{-1}. The fits to the symmetric (red) and antisymmetric (green) stretches as well as the cumulative fit (blue) are shown.

As before, fits of this nature were obtained for all of the background-subtracted data. Table 4.4 lists the fitting parameters obtained for the symmetric stretch for all of the spectra, the values in parenthesis are the fit errors.

Table 4.4: Voigt fitting parameters (with fit errors) for the symmetric stretch from the TIR-Raman data.

C	y_0	ω_0 (cm^{-1})	FWHM (cm^{-1})	Area	W_g (cm^{-1})	W_l (cm^{-1})	R^2
			pH 5				
150	69 (4)	838.6 (0.2)	18.4 (0.8)	38000 (1000)	5 (3)	17 (2)	0.85278
200	197 (4)	838.6 (0.2)	18.8 (0.8)	41000 (1000)	11 (2)	12 (2)	0.89376
250	61 (5)	838.8 (0.2)	20.9 (0.5)	43000 (1000)	20.9 (0.5)	0	0.88539
300	156 (5)	838.3 (0.1)	18.2 (0.4)	65000 (2000)	11.7 (1)	10.4 (1)	0.95271
350	125 (5)	838.4 (0.1)	18.5 (0.3)	90000 (2000)	9 (1)	14.1 (0.8)	0.96743
			pH 6				
150	33 (4)	838.0 (0.3)	20.0 (0.9)	33000 (2000)	12 (3)	13 (2)	0.81059
200	26 (4)	838.1 (0.2)	17.8 (0.5)	33000 (1000)	15 (1)	5 (2)	0.89071
250	33 (5)	837.9 (0.2)	19.8 (0.5)	64000 (2000)	7 (2)	17 (1)	0.93759
300	194 (5)	837.4 (0.2)	19.6 (0.5)	83000 (2000)	0	19.4 (0.4)	0.93778
350	197 (5)	837.9 (0.1)	18.5 (0.4)	87000 (2000)	7 (1)	15.5 (0.7)	0.96628
			pH 7				
150	-251 (4)	838.7 (0.3)	16.9 (0.8)	21000 (1000)	14 (2)	5 (3)	0.70108
200	-4 (5)	837.8 (0.2)	17.6 (0.7)	44000 (2000)	6 (3)	15 (2)	0.86349
250	-103 (6)	837.4 (0.2)	17.7 (0.6)	50000 (2000)	9 (2)	12 (2)	0.89153
300	-151 (4)	838.3 (0.1)	18.0 (0.4)	50000 (2000)	16.0 (1)	4 (1)	0.93751
350	-115 (5)	838.2 (0.1)	18.6 (0.3)	71000 (2000)	14.0 (0.9)	8 (1)	0.96157

While the R^2 may give one cause to question the fitting, they are artificially low due to the noise in the edge regions of the fit. Another factor that hinders the fitting is the fact that some spectra have an artifact at 800 cm^{-1} from the top of the silica mode. Unfortunately, this is difficult to deal with, and will be a hindrance so long as the peaks of interest overlap with the silica modes. From the above table, a few plots were constructed to see if a pattern exists that would indicate some form of adsorption. One such plot, that of peak area versus concentration, is shown in Figure 4.17. As before, y_0 was set to zero as the spectra have had a background-subtracted from them, therefore, zero concentration will have zero scattering intensity.

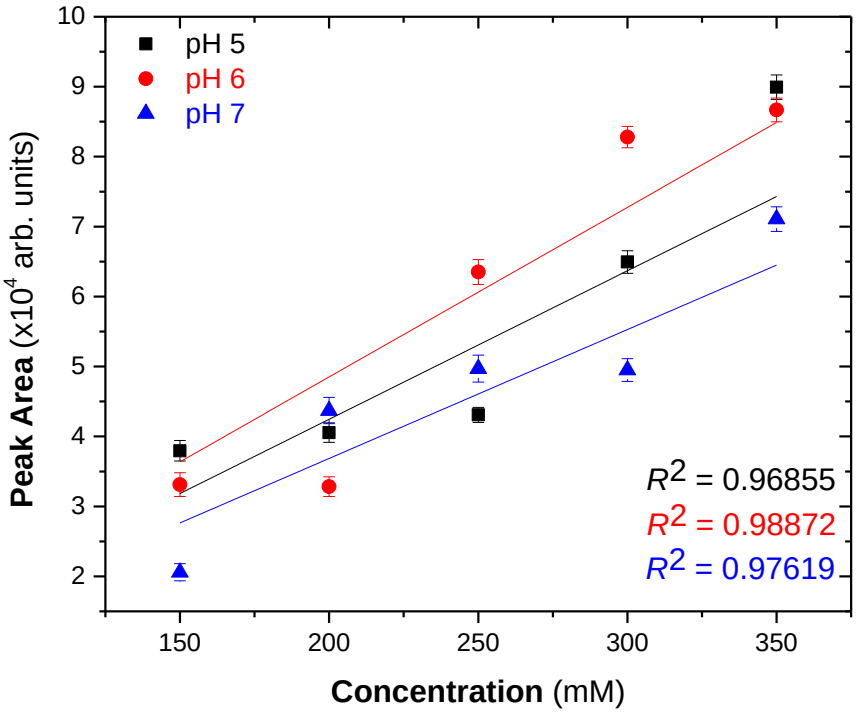

Figure 4.17: Peak area of the symmetric stretch vs. concentration for the three solution sets. The data was linearly fit, setting $y_0 = 0$.

Although they may not look it, the plots are fairly linear as indicated by the decent R^2 values. The plots are not as nicely linear as were those of the conventional data, and there are a few reasons as to why this is the case. The biggest reason is that the signal-to-noise ratio is much better for the conventional data. The difference in intensity is quite noticeable when comparing conventional and TIR data. For example, the symmetric stretch in the pH 5 150 mM conventional spectrum is approximately 4500 counts tall, whereas the same peak in the TIR data is a mere 1600 counts tall (Figure 4.14). This sheer size difference makes fitting the spectra vastly more difficult for the TIR data. Another thing affecting the peak area is the difficulty in subtracting the background cleanly, as evidenced by the artifacts present in various spectra from the large silica 800 cm^{-1} mode. This artifact can give a negative or positive deviation to the spectrum which of course affects the fitting leading to a relative non-linearity of the TIR data compared to the conventional data in which there is no silica mode artifact.

The following plots are used to compare the center frequency of the symmetric stretching mode across the concentrations and pHs. The first of which compares the center frequency versus concentration to determine if a shift occurs in the TIR spectrum with increasing concentration.

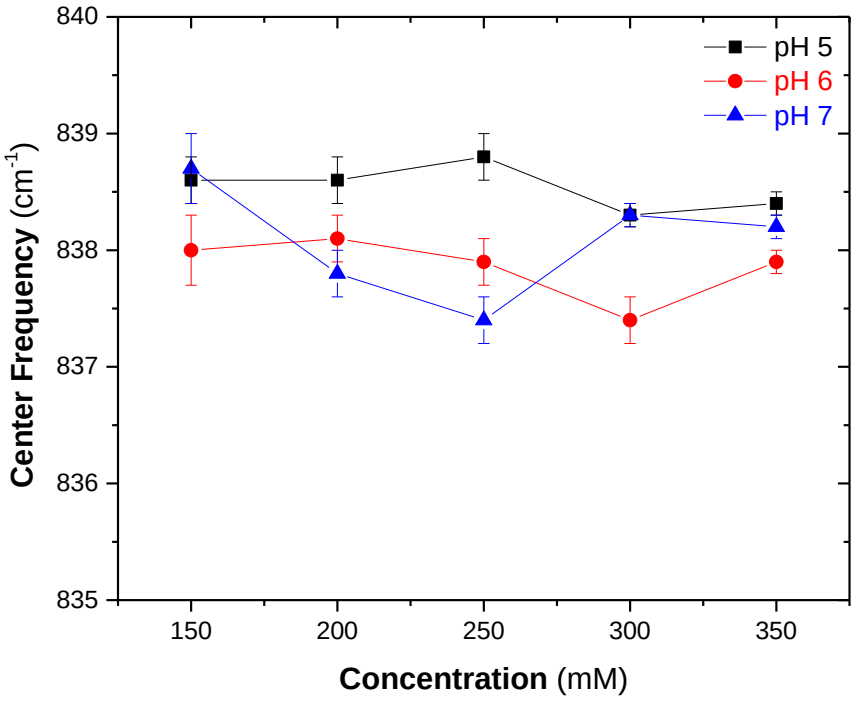

Figure 4.18: Center frequency of the symmetric stretch vs. concentration for pH.

From Figure 4.18, one will notice that there is no peak shift that occurs with concentration. The center frequency "shifts" over a range of 2 cm^{-1}, well within experimental error, and these shifts occur with no distinct pattern. The center frequency seems to jump randomly over this small range, this leads to one determining that there is no "real" shift of which to be concerned. Ergo, the peak position is relatively constant with increasing concentration, as it was for the conventional data. There is a small shift compared to the conventional data, as the center frequencies were higher, but even this shift is only on the order of 5 cm^{-1}, still within experimental error, and still such a small shift that it is likely meaningless. Figure 4.19 helps to emphasize this point, as it is a graph of center frequency versus pH for the five concentrations.

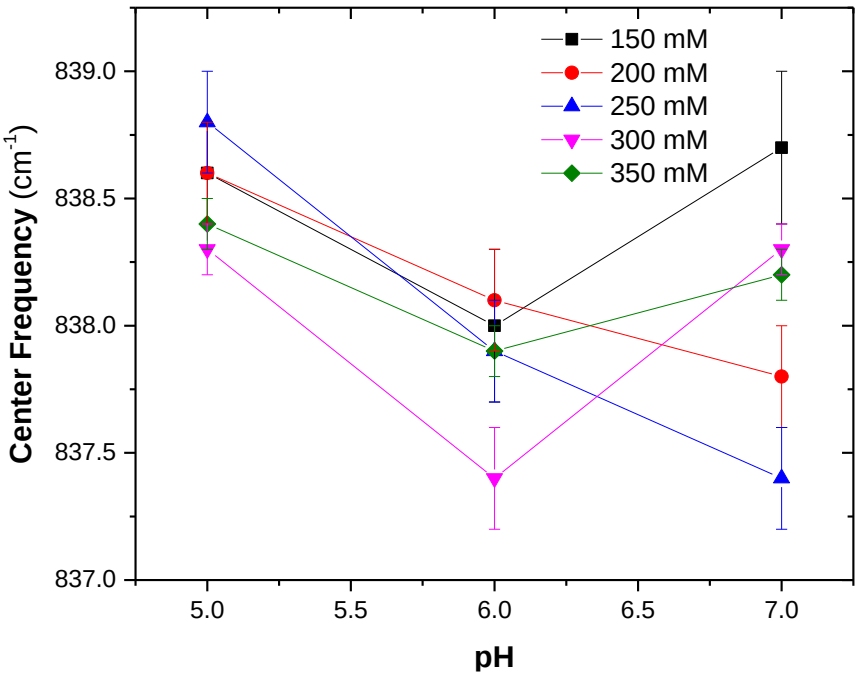

Figure 4.19: Center frequency of the symmetric stretch vs. pH for each concentration.

From Figure 4.19, note that for three of the concentrations there does not appear to be a trend, but for the 200 and 250 mM, there is a constant decrease with increasing pH. However, the range over which this occurs is very small, ~2 cm^{-1}, and it only occurs for these two concentrations. As the range is within experimental error, and is not similar for all concentrations, it is likely that this "trend" is, again, meaningless.

In the background-subtracted spectra shown above, there is one strong peak which is associated with the symmetric stretching mode of selenate. This peak position agrees well with the conventional data, which, in turn agrees with literature values for conventional Raman spectra of selenate. The fact that there is only one peak shown indicates that there is no reduction of symmetry of the selenate anion. This means that selenate retains its tetrahedral structure, which leads one to assume a lack of adsorption to

the silica surface. If there was adsorption occurring, one would see the symmetric stretching mode split into either two peaks (C_{3v}, monodentate adsorption), or into three peaks (C_{2v}, bidentate adsorption). The single peak is indicative of the T_d point group as shown previously with the character tables of the three discussed point groups (Figures 2.2 – 2.4). This symmetry based argument is supported by the linearity of the peak area versus concentration plots, as one would expect a linear trend unless there was adsorption. Also, the peak position versus concentration and pH plots support the lack of adsorption as there is little to no shift occurring in the peak position. These things along with the lack of splitting all point to there being no adsorption of selenate to the silica surface over the pH range of 5 to 7.

4.2 Selenite

4.2.1 Bulk Raman Spectra of Selenite Solutions

The Raman spectrum of a pH adjusted, 1 M NaCl solution in nanopure water was collected to be used as a background. These spectra were acquired in a slightly different manner than the selenate conventional spectra, as a glass vial was used in place of the quartz cuvette, thus leading to a differently shaped background. This raw spectrum along with the raw spectra of the five Na_2SeO_3 pH 6 solutions are shown in Figure 4.23.

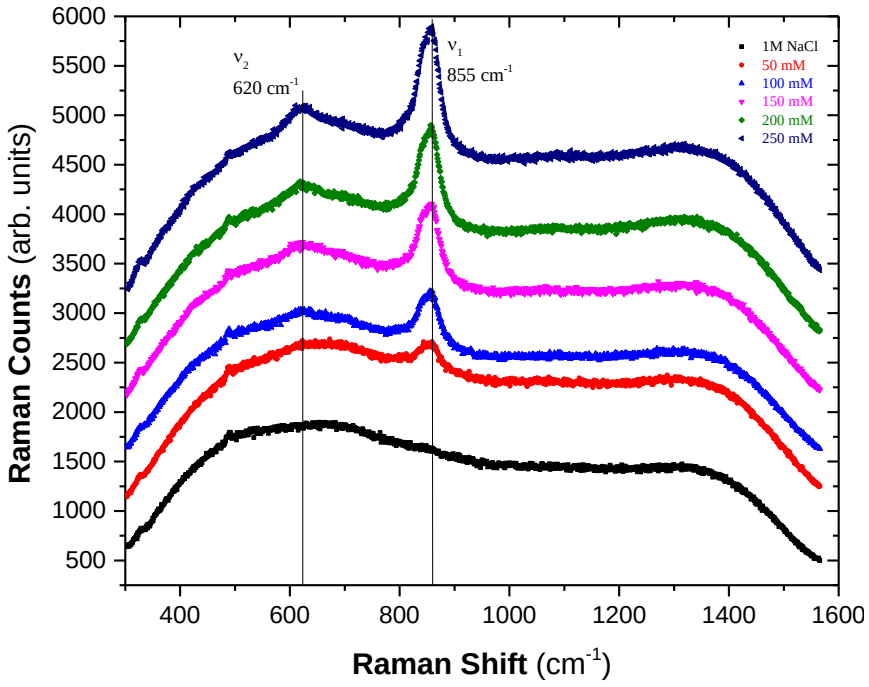

Figure 4.20: Raw Raman spectra of a pH 6 1 M NaCl solution and five Na_2SeO_3 solutions of varying concentration and also with 1 M NaCl.

Note the large background from the glass vial, and the otherwise featureless spectrum of the background solution. The main feature of the selenite spectra is the large peak at ~857 cm^{-1}. Considering the speciation of the selenite anion at this pH one will find that it exists almost completely in the protonated biselenite ($HSeO_3^-$) form. Considering this, the large peak is attributed to the symmetric stretching mode (ν_{ss}) of the $HSeO_3^-$ ion in solution.[45] Another feature is the small, broad peak at ~620 cm^{-1}, which is attributed to the scissoring mode.[45] Figure 4.21 shows the background-subtracted spectra of these same solutions. This subtraction was done for clarity in determining peak positions. The *x*-axis of this was also altered to bring more focus to the area of interest (500-1200 cm^{-1}). The background-subtracted spectra of the pH 7 solutions are also shown.

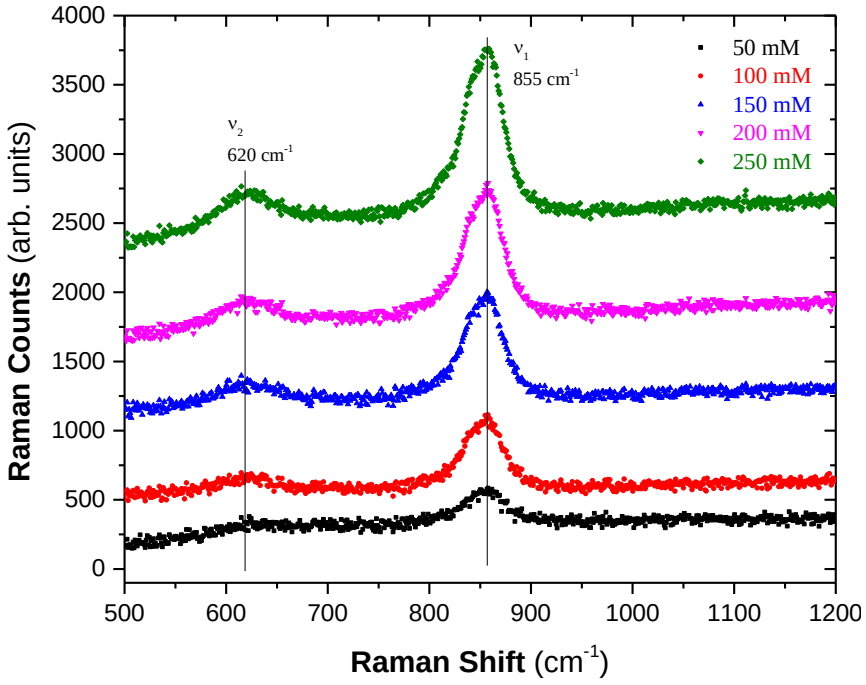

Figure 4.21: Background-subtracted conventional Raman spectra of pH 6 Na_2SeO_3 solutions.

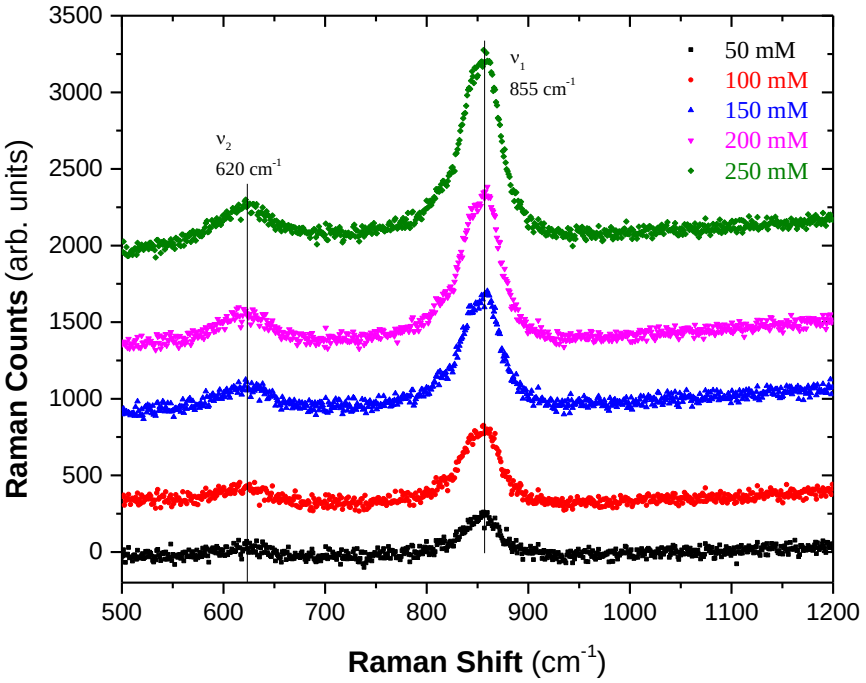

Figure 4.22: Background-subtracted spectra of the pH 7 Na_2SeO_3 solutions.

4.2.2 TIR-Raman of Selenite Solutions on Silica

Figure 4.23a, and b present the background-subtracted TIR-Raman spectra of pH 6 and 7 Na_2SeO_3 on silica. Note the large feature at approximately 860 cm^{-1}, as with the conventional data, this corresponds to the symmetric stretching mode.

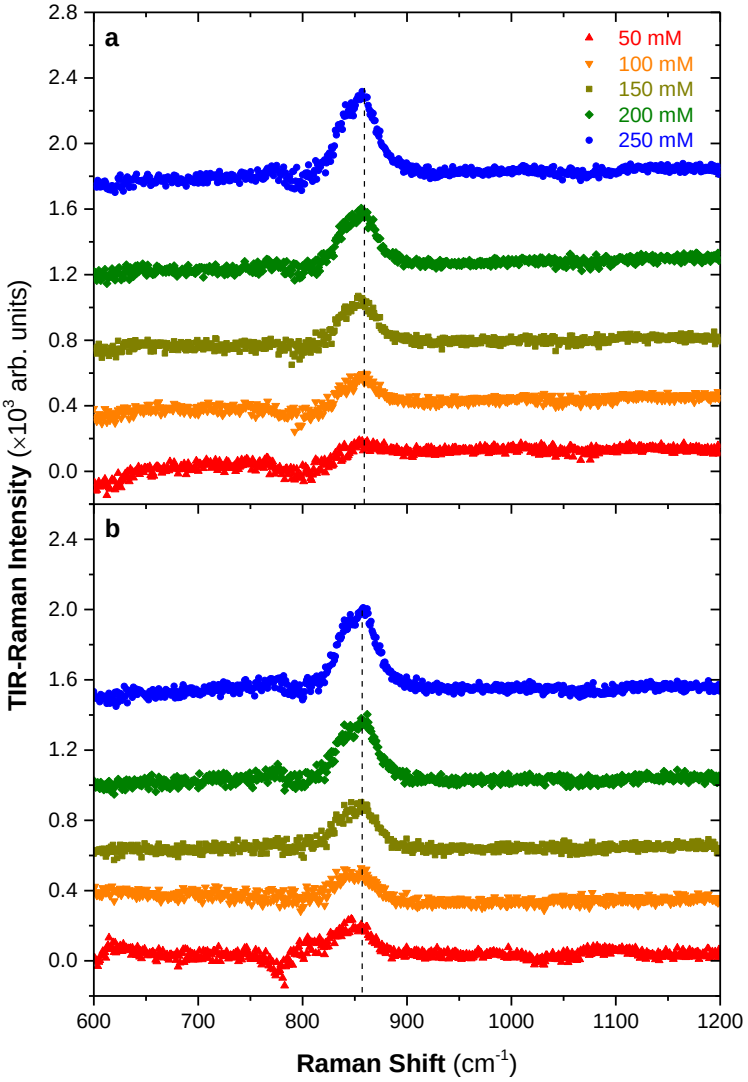

Figure 4.23: TIR-Raman spectra of a) pH 6 and b) pH 7 Na_2SeO_3 solutions on silica.

Based on the spectra in Figure 4.23, one may tentatively say that there is no adsorption occurring at the silica-aqueous interface as there is no reduction of symmetry causing a splitting of this peak. However, as attempts to duplicate this data were unsuccessful, a definitive answer may not be obtained. Figure 4.24 shows the attempts at duplication of the pH 7 TIR data; pH 6 attempts are not shown.

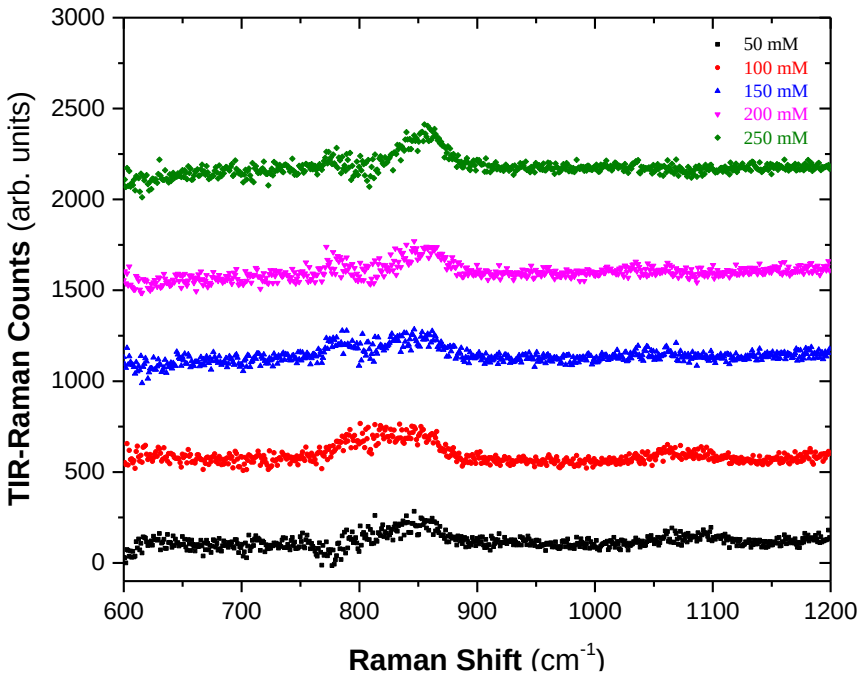

Figure 4.24: Attempts to duplicate the TIR-Raman data for Na_2SeO_3 on silica.

While there does appear to be a peak around 860 cm^{-1}, it is barely discernible from the noise, and compared to the previous data, the signal is quite low. The artifact at 800 cm^{-1} is approximately the same size as the "peak" which gives reason to doubt the spectra. It is unclear exactly as to why the initial data was successfully obtained, but any attempts

at duplication failed. There are a number of complications surrounding selenite as a whole that could have contributed. One major factor is that the solutions had a beige-colored appearance. This coloring reflects a changes in the index of refraction of the solution which can have a dramatic effect on the spectra. However, this should have also been a problem for the initial data as well, leading one to believe this was not the cause. Another possible problem could have been the oxidation of selenite into selenate in the initial solutions which were a bit old at the time the data was collected compared to the duplication attempts which utilized freshly made solutions. However, this is also not likely the cause as if oxidation had occurred, the peak in the initial data set would have shifted to approximately 840 cm^{-1}, and the data would look like that of the selenate experiment. As this also did not happen, one may rule out oxidation of the original solutions as a reason for why they worked, and attempts at duplication did not. As aforesaid, it is unclear as to why the experiment initially worked only to have any duplication attempts fail.

At this point "spot check" solutions were made to ensure the system itself was not the problem. These solutions include 250 mM sodium salts of selenate, selenite, sulfate, and sulfite, and also a 500 mM solution of sodium sulfate. These solutions were not adjusted for pH or given a background electrolyte. Figure 4.25 shows the TIR-Raman spectra of these various solutions.

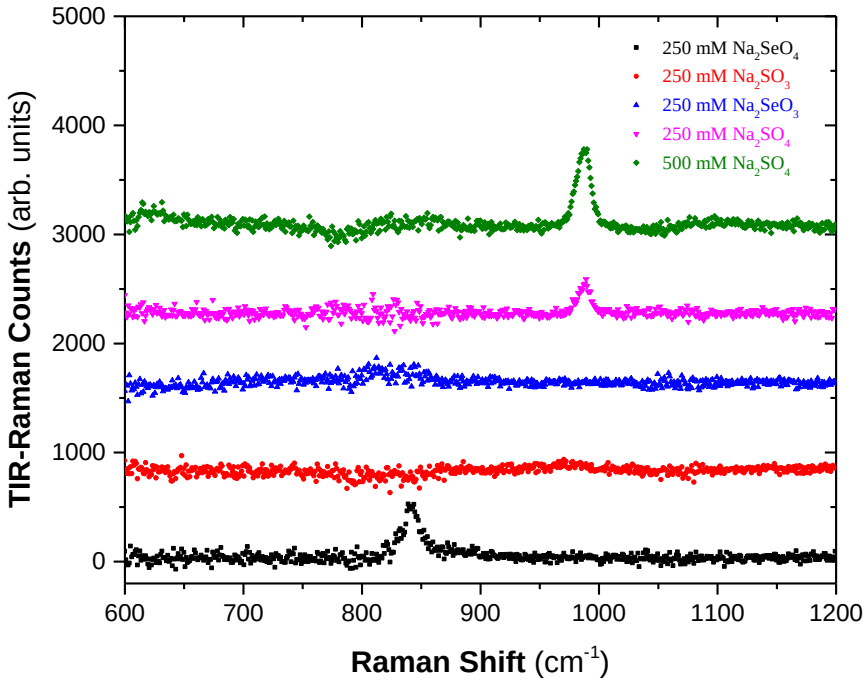

Figure 4.25: TIR-Raman spectra of the various "spot check" solutions on silica.

From spectra in Figure 4.25, one can see that the two tetrahedral oxyanions produced clean spectra, whereas the two C_{3v} oxyanions gave no signal. From these spectra it was determined that it may not have been a problem with the system, yet something intrinsic to selenite itself as sulfite was also not visible. It was at this point that it was noted that although selenite does not produce a viable spectrum, selenate does; indicating that selenate must have a much greater propensity for Raman scattering, and the selenate experiment mentioned above was performed. It is still unclear as to why the experiment worked initially, and more work is needed to determine exactly what was occurring to cause such an anomaly.

CHAPTER 5: CONCLUSIONS AND FUTURE WORK

To conclude, it was found that there is no discernible adsorption occurring at the silica-aqueous interface of the toxic oxyanion selenate. This was investigating utilizing TIR-Raman spectroscopy analogous to measurements performed previously by Jubb and co-workers.[40] The results were examined utilizing basic group theory to investigate the possibility of a reduction of the symmetry of the bulk oxyanion. This lowering of symmetry would have resulted in the symmetric stretching mode splitting into two or three separate peaks whether a monodentate or bidentate binding geometry occurred respectively. As shown in Figures 4.13-4.15, the symmetric stretch does not show any splitting into multiple peaks, meaning that adsorption does not occur as a tetrahedral geometry dominates. Also, considering the PZC of silica, the results of this experiment make sense as it would be remarkable if a negatively charged ion were to adsorb to a negative surface. These results then imply that as selenate is not being adsorbed by silica; that in the environment, the major component of the Earth's crust is doing nothing to hamper the mobility of this anion. This will be especially true in areas where the crust is particularly rich in silica as opposed to other minerals. This mobility will give selenate enhanced bioavailability as it will be capable of reaching ground water if not adsorbed in transit. This will pose a toxicity problem as, although less toxic than selenite, selenate concentration reach elevated and possibly toxic levels.

There are a number of upgrades that could allow for better control of the probing depth, better signal-to-noise ratio, easier alignment, and easier data collection overall. One of the major issues with the current system is the large feature of silica at 800 cm^{-1}. This can be overcome by utilizing hemispheres made from a material that does not have this feature such as cubic zirconia, sapphire, and even diamond. Another improvement that could be made is just an overall upgrade to the sample cell and its mounting assembly. At the moment, the cell is moveable, which is useful at times, however, due to its construction, it is difficult to ensure that the cell does not move if bumped even gently. Once moved, it is extremely difficult to ensure the cell is returned to its original position as there is only a single screw fixing it to the mount, about which the cell may spin. The idea would be for the cell to be mounted on a single post, and, once in place, not moved as the rest of the system would be re-aligned around the cells new position. In the long-term, another laser may be used to increase the signal, a shorter wavelength will enhance Raman scattering, increasing the overall signal. A goniometer may be added to give precise control over the arm on which the last mirror and focusing lens lie, this would allow for greater control of the incidence angle, and an easier method by which the incidence angle may be obtained. These modifications may also allow for obtaining and duplicating TIR-Raman spectra of selenite as attempts at duplication were not successful with the current system.

The work performed herein will also serve as a standard to which future experiments may be compared, acting as a control for the study of selenate adsorption to various mineral oxides such as hematite, goethite, gibbsite, etc. This method may also now be applied to other oxyanions as well such as chlorate, carbonate, phosphate, etc. In the long term, the

hope is that this method will be utilized to investigate a range of oxyanions adsorbing to multiple mineral surfaces. This will be performed by coating the existing hemispheres with a thin film of the mineral of interest, and running the experiment in similar fashion to what has been done. There is also the potential to utilize this system to investigate the formation of ternary complexes at the surface in the presence of various metal cations (Pb^{2+}, Cd^{2+}, etc.).

REFERENCES

1. Deutsch, W. J., *Groundwater Geochemistry: Fundamentals and Applications to Contamination*; CRC Press: Boca Raton, FL, 1997, p 221.
2. Perez, C.; Antelo, J.; Fiol, S.; Arce, F., Modeling Oxyanion Adsorption on Ferralic Soil, Part 1: Parameter Validation with Phosphate Ion. *Environ. Toxicol. Chem.* **2014**, *33*, 2208-2216.
3. Perez, C.; Antelo, J.; Fiol, S.; Arce, F., Modeling Oxyanion Adsorption on Ferralic Soil, Part 2: Chromate, Selenate, Molybdate, and Arsenate Adsorption. *Environ. Toxicol. Chem.* **2014**, *33*, 2217-2224.
4. Neupane, G.; Donahoe, R. J.; Arai, Y., Kinetics of Competitive Adsorption/Desorption of Arsenate and Phosphate at the Ferrihydrite-Water Interface. *Chem. Geol.* **2014**, *368*, 31-38.
5. Vasileva, E.; Hadjiivanov, K.; Mandjukov, P., Adsorption of Cr^{6+} Oxo Anions on Pure and Peroxide-Modified TiO_2 (Anatase). *Colloid Surf. A* **1994**, *90*, 9-15.
6. Stachowicz, M.; Hiemstra, T.; van Riemsdijk, W. H., Multi-Competitive Interaction of As(III) and As(V) Oxyanions with Ca^{2+}, Mg^{2+}, PO_4^{3-}, and CO_3^{2-} Ions on Goethite. *J. Colloid Interface Sci.* **2008**, *320*, 400-414.
7. Lefevre, G., In Situ Fourier-Transform Infrared Spectroscopy Studies of Inorganic Ions Adsorption on Metal Oxides and Hydroxides. *Adv. Colloid Interface Sci.* **2004**, *107*, 109-123.
8. Zhuravlev, L. T., The Surface Chemistry of Amorphous Silica. Zhuravlev Model. *Colloid Surf. A* **2000**, *173*, 1-38.
9. Sulpizi, M.; Gaigeot, M. P.; Sprik, M., The Silica-Water Interface: How the Silanols Determine the Surface Acidity and Modulate the Water Properties. *J. Chem. Theory Comput.* **2012**, *8*, 1037-1047.
10. Ong, S. W.; Zhao, X. L.; Eisenthal, K. B., Polarization of Water Molecules at a Charged Interface - 2nd Harmonic Studies of the Silica Water Interface. *Chem. Phys. Lett.* **1992**, *191*, 327-335.
11. Leung, K.; Nielsen, I. M. B.; Criscenti, L. J., Elucidating the Bimodal Acid-Base Behavior of the Water-Silica Interface from First Principles. *J. Am. Chem. Soc.* **2009**, *131*, 18358-18365.
12. Rimola, A.; Costa, D.; Sodupe, M.; Lambert, J. F.; Ugliengo, P., Silica Surface Features and Their Role in the Adsorption of Biomolecules: Computational Modeling and Experiments. *Chem. Rev.* **2013**, *113*, 4216-4313.
13. Wang, X. F.; Zhao, M.; Nolte, D. D., Ambient Molecular Water Accumulation on Silica Surfaces Detected by a Reflectance Interference Optical Balance. *Appl. Phys. Lett.* **2010**, *97*.
14. Gouveia, R. F.; Costa, C. A. R.; Galembeck, F., Water Vapor Adsorption Effect on Silica Surface Electrostatic Patterning. *J. Phys. Chem. C* **2008**, *112*, 17193-17199.

15. Mahadevan, T. S.; Garofalini, S. H., Dissociative Chemisorption of Water onto Silica Surfaces and Formation of Hydronium Ions. *J. Phys. Chem. C* **2008**, *112*, 1507-1515.
16. Mazurenka, M.; Hamilton, S. M.; Unwin, P. R.; Mackenzie, S. R., In Situ Measurement of Colloidal Gold Adsorption on Functionalized Silica Surfaces. *J. Phys. Chem. C* **2008**, *112*, 6462-6468.
17. Gomoyunova, M. V.; Malygin, D. E.; Pronin, I. I., Interaction of Iron Atoms with the Oxidized Silicon Surface. *Tech. Phys.* **2006**, *51*, 1243-1246.
18. Donose, B. C.; Vakarelski, I. U.; Higashitani, K., Silica Surfaces Lubrication by Hydrated Cations Adsorption from Electrolyte Solutions. *Langmuir* **2005**, *21*, 1834-1839.
19. Wang, X. K.; Dong, W. M.; Zhang, H. X.; Tao, Z. Y., A Multitracer Study on the Adsorption of 36 Elements on a Silica: Effects of pH and Fulvic Acid. *J. Radioanal. Nucl. Chem.* **2001**, *250*, 491-496.
20. Polyshchuk, L. N.; Yanovskaya, E. S.; Yanishpol'skii, V. V.; Tertykh, V. A.; Sukhoi, K. M.; Burmistr, M. V., Sorption of Mo(VI), W(VI), Cr(VI), and V(V) Anions on a Silica Gel Modified with Immobilized Polyionene. *Russ. J. Appl. Chem.* **2007**, *80*, 1590-1593.
21. Mallard, G. E.; Aronson, D. A. *US Geological Survey Toxic Substance Hydrology Program--Proceedings of the Technical Meeting, Monterey, California, March 11-15, 1991*; 1991; pp 319-323.
22. Hamilton, S. J., Hazard Assessment of Inorganics to 3 Endangered Fish in the Green-River, Utah. *Ecotoxicol. Environ. Safety* **1995**, *30*, 134-142.
23. Hamilton, S. J.; Buhl, K. J., Hazard Evaluation of Inorganics, Singly and in Mixtures, to Flannelmouth Sucker *Catostomus Latipinnis* in the San Juan River, New Mexico. *Ecotoxicol. Environ. Safety* **1997**, *38*, 296-308.
24. Geoffroy, L.; Gilbin, R.; Simon, O.; Floriani, M.; Adam, C.; Pradines, C.; Cournac, L.; Garnier-Laplace, J., Effect of Selenate on Growth and Photosynthesis of *Chlamydomonas Reinhardtii*. *Aquat. Toxicol.* **2007**, *83*, 149-158.
25. Duan, L. Q.; Song, J. M.; Li, X. G.; Yuan, H. M.; Xu, S. S., Distribution of Selenium and Its Relationship to the Eco-Environment in Bohai Bay Seawater. *Mar. Chem.* **2010**, *121*, 87-99.
26. Torres, J.; Pintos, V.; Gonzatto, L.; Dominguez, S.; Krerner, C.; Kremer, E., Selenium Chemical Speciation in Natural Waters: Protonation and Complexation Behavior of Selenite and Selenate in the Presence of Environmentally Relevant Cations. *Chem. Geol.* **2011**, *288*, 32-38.
27. Floor, G. H.; Calabrese, S.; Roman-Ross, G.; D'Alessandro, W.; Aiuppa, A., Selenium Mobilization in Soils Due to Volcanic Derived Acid Rain: An Example from Mt Etna Volcano, Sicily. *Chem. Geol.* **2011**, *289*, 235-244.
28. Floor, G. H.; Iglesias, M.; Roman-Ross, G.; Corvini, P. F. X.; Lenz, M., Selenium Speciation in Acidic Environmental Samples: Application to Acid Rain-Soil Interaction at Mount Etna Volcano. *Chemosphere* **2011**, *84*, 1664-1670.
29. Peak, D.; Sparks, D. L., Mechanisms of Selenate Adsorption on Iron Oxides and Hydroxides. *Environ. Sci. Technol.* **2002**, *36*, 1460-1466.

30. Yamani, J. S.; Lounsbury, A. W.; Zimmerman, J. B., Adsorption of Selenite and Selenate by Nanocrystalline Aluminum Oxide, Neat and Impregnated in Chitosan Beads. *Water Res.* **2014**, *50*, 373-381.
31. Duc, M.; Lefevre, G.; Fedoroff, M.; Jeanjean, J.; Rouchaud, J. C.; Monteil-Rivera, F.; Dumonceau, J.; Milonjic, S., Sorption of Selenium Anionic Species on Apatites and Iron Oxides from Aqueous Solutions. *J. Environ. Radioactiv.* **2003**, *70*, 61-72.
32. Catalano, J. G.; Zhang, Z.; Fenter, P.; Bedzyk, M. J., Inner-Sphere Adsorption Geometry of Se(IV) at the Hematite (100)-Water Interface. *J. Colloid Interface Sci.* **2006**, *297*, 665-671.
33. Rovira, M.; Gimenez, J.; Martinez, M.; Martinez-Llado, X.; de Pablo, J.; Marti, V.; Duro, L., Sorption of Selenium(IV) and Selenium(VI) onto Natural Iron Oxides: Goethite and Hematite. *J. Hazard. Mater.* **2008**, *150*, 279-284.
34. Goldberg, S., Macroscopic Experimental and Modeling Evaluation of Selenite and Selenate Adsorption Mechanisms on Gibbsite. *Soil Sci. Soc. Am. J.* **2014**, *78*, 473-479.
35. Ingle Jr., J. D.; Crouch, S. R., *Spectrochemical Analysis*; Prentice-Hall: Upper Saddle River, NJ, 1988, p 590.
36. Bernath, P. F., *Spectra of Atoms and Molecules*, 2nd ed.; Oxford University Press: New York, NY, 2005, p 439.
37. Woods, D. A.; Bain, C. D., Total Internal Reflection Raman Spectroscopy. *Analyst* **2012**, *137*, 35-48.
38. Atkins, P.; Overton, T.; Rourke, J.; Weller, M.; Armstrong, F.; Hagerman, M., *Inorganic Chemistry*, 5th ed.; Oxford University Press: Great Britain, 2010, p 824.
39. Hug, S. J., In Situ Fourier Transform Infrared Measurements of Sulfate Adsorption on Hematite in Aqueous Solutions. *J. Colloid Interface Sci.* **1997**, *188*, 415-422.
40. Jubb, A. M.; Verreault, D.; Posner, R.; Criscenti, L. J.; Katz, L. E.; Allen, H. C., Sulfate Adsorption at the Buried Hematite/Solution Interface Investigated Using Total Internal Reflection (TIR)-Raman Spectroscopy. *J. Colloid. Interface Sci.* **2013**, *400*, 140-146.
41. CRC Handbook of Chemistry and Physics. 95th (Internet Version 2015) ed.; Haynes, W. M., Ed. CRC Press/Taylor and Francis: Boca Raton, FL, 2015.
42. Ganesan, A. S., Raman Effect in Selenic Acid and Some Selenates. *Proc. Indian Acad. Sci. A: Math. Sci.* **1934**, *1*, 156-162.
43. Walrafen, G. E., Raman Spectral Studies of Aqueous Solutions of Selenic Acid. *J. Chem. Phys.* **1963**, *39*, 1479-1492.
44. Ben Mabrouk, K.; Kauffmann, T. H.; Aroui, H.; Fontana, M. D., Raman Study of Cation Effect on Sulfate Vibration Modes in Solid State and in Aqueous Solutions. *J. Raman Spectros.* **2013**, *44*, 1603-1608.
45. Venkateswaran, C. S., The Raman Spectra of Selenious Acid and Its Sodium Salts. *Proc. Indian Acad. Sci. A: Math. Sci.* **1936**, *3*, 533-543.

APPENDIX A
COPYRIGHT INFORMATION FOR FIGURE 2.3

ROYAL SOCIETY OF CHEMISTRY LICENSE TERMS AND CONDITIONS

Jun 24, 2014

This is a License Agreement between Brant M Finzer ("You") and Royal Society of Chemistry ("Royal Society of Chemistry") provided by Copyright Clearance Center ("CCC"). The license consists of your order details, the terms and conditions provided by Royal Society of Chemistry, and the payment terms and conditions.

All payments must be made in full to CCC. For payment instructions, please see information listed at the bottom of this form.

License Number	3415391387831
License date	Jun 24, 2014
Licensed content publisher	Royal Society of Chemistry
Licensed content publication	Analyst
Licensed content title	Total internal reflection Raman spectroscopy
Licensed content author	David A. Woods,Colin D. Bain
Licensed content date	Oct 14, 2011
Volume number	137
Issue number	1
Type of Use	Thesis/Dissertation
Requestor type	academic/educational
Portion	figures/tables/images
Number of figures/tables/images	1
Format	print and electronic
Distribution quantity	10
Will you be translating?	no
Order reference number	None
Title of the thesis/dissertation	Total Internal Reflection Raman Spectroscopy for the Detection of Oxyanion Adsorption to a Mineral Thin-Film
Expected completion date	Aug 2014
Estimated size	100
Total	0.00 USD

Terms and Conditions

This License Agreement is between {Requestor Name} ("You") and The Royal Society of Chemistry ("RSC") provided by the Copyright Clearance Center ("CCC"). The license consists of your order details, the terms and conditions provided by the Royal Society of Chemistry, and the payment terms and conditions.